Astronomy & Astrophysics manuscript no. eros-gsa
February 12, 2022

The EROS2 search for microlensing events towards the spiral arms: the complete seven season results

Y.R. Rahal[1⋆], C. Afonso[2⋆⋆], J.-N. Albert[1], J. Andersen[3], R. Ansari[1], É. Aubourg[2⋆⋆⋆], P. Bareyre[2], J.-P. Beaulieu[4], X. Charlot[2], F. Couchot[1], C. Coutures[2,4], F. Derue[1†], R. Ferlet[4], P. Fouqué[7,8], J.-F. Glicenstein[2], B. Goldman[2‡], A. Gould[5], D. Graff[5§], M. Gros[2], J. Haïssinski[1], C. Hamadache[2¶], J. de Kat[2], É. Lesquoy[2,4], C. Loup[4], L. Le Guillou[2‖], C. Magneville[2], B. Mansoux[1], J.-B. Marquette[4], É. Maurice[6], A. Maury[8⋆⋆], A. Milsztajn[2††], M. Moniez[1], N. Palanque-Delabrouille[2], O. Perdereau[1], S. Rahvar[9], J. Rich[2], M. Spiro[2], P. Tisserand[2‡‡], A. Vidal-Madjar[4], The EROS-2 collaboration

[1] Laboratoire de l'Accélérateur Linéaire, IN2P3-CNRS, Université de Paris-Sud, B.P. 34, 91898 Orsay Cedex, France
[2] CEA, DSM, DAPNIA, Centre d'Études de Saclay, 91191 Gif-sur-Yvette Cedex, France
[3] The Niels Bohr Institute, Astronomy Group, Juliane Maries vej 30, DK - 2100 Copenhagen, Denmark
[4] Institut d'Astrophysique de Paris, UMR 7095 CNRS, Université Pierre & Marie Curie, 98 bis Boulevard Arago, 75014 Paris, France
[5] Department of Astronomy, Ohio State University, Columbus, Ohio 43210, U.S.A.
[6] Observatoire de Marseille, INSU-CNRS, 2 place Le Verrier, 13248 Marseille Cedex 04, France
[7] Observatoire Midi-Pyrénées, LATT, Université de Toulouse, CNRS, 14 av. E. Belin, F-31400 Toulouse, France
[8] European Southern Observatory (ESO), Casilla 19001, Santiago 19, Chile
[9] Dept. of Physics, Sharif University of Technology, Tehran, Iran

Received ??/??/2008, accepted

ABSTRACT

Aims. The EROS-2 project has been designed to search for microlensing events towards any dense stellar field. The densest parts of the Galactic spiral arms have been monitored to maximize the microlensing signal expected from the stars of the Galactic disk and bulge.

Methods. 12.9 million stars have been monitored during 7 seasons towards 4 directions in the Galactic plane, away from the Galactic center.

Results. A total of 27 microlensing event candidates have been found. Estimates of the optical depths from the 22 best events are provided. A first order interpretation shows that simple Galactic models with a standard disk and an elongated bulge are in agreement with our observations. We find that the average microlensing optical depth towards the complete EROS-cataloged stars of the spiral arms is $\bar{\tau} = 0.51 \pm .13 \times 10^{-6}$, a number that is stable when the selection criteria are moderately varied. As the EROS catalog is almost complete up to $I_C = 18.5$, the optical depth estimated for the sub-sample of bright target stars with $I_C < 18.5$ ($\bar{\tau} = 0.39 \pm .11 \times 10^{-6}$) is easier to interpret.

Conclusions. The set of microlensing events that we have observed is consistent with a simple Galactic model. A more precise interpretation would require either a better knowledge of the distance distribution of the target stars, or a simulation based on a Galactic model. For this purpose, we define and discuss the concept of optical depth for a given catalog or for a limiting magnitude.

Key words. Cosmology: dark matter - Galaxy: disk - Galaxy: bulge - Galaxy: structure - Galaxy: spiral arms - Galaxy: microlensing

1. Introduction

After the first reports of microlensing candidates (Aubourg *et al.* 1993, Alcock *et al.* 1993, Udalski *et al.* 1993), the EROS team has performed extensive microlensing surveys from 1996 to 2003, that monitored the Magellanic clouds and large regions in the Galactic plane. The EROS-2 search for lensing towards the Magellanic clouds (Tisserand *et al.* 2007)

Send offprint requests to: M. Moniez, e-mail: moniez@lal.in2p3.fr
see also our WWW server at URL :
http://www.lal.in2p3.fr/recherche/eros

⋆ Now at Electronics Arts Canada, Vancouver, Canada
⋆⋆ Now at Max-Planck-Institut für Astronomie, Koenigstuhl 17, D-69117 Heidelberg, Germany
⋆⋆⋆ Also at APC, 10 rue Alice Domon et Lonie Duquet, F-75205 Paris Cedex 13, France
† Now at LPNHE, 4 place Jussieu, F-75252 Paris Cedex 5, France
‡ Now at Max-Planck-Institut für Astronomie, Koenigstuhl 17, D-69117 Heidelberg, Germany
§ Now at Division of Medical Imaging Physics, Johns Hopkins University Baltimore, MD 21287-0859, USA
¶ Also at CSNSM, Universit Paris Sud 11, IN2P3-CNRS, 91405 Orsay Campus, France
‖ Now at LPNHE, 4 place Jussieu, F-75252 Paris Cedex 5, France
⋆⋆ Now at San Pedro de Atacama Celestial Exploration, Casilla 21, San Pedro de Atacama, Chile
†† Deceased
‡‡ Now at Mount Stromlo Observatory, Weston P.O., ACT, 2611, Australia

yielded significant upper limits on the fraction of the Milky Way halo that can be comprised of dark objects with masses between $10^{-7}M_\odot$ and $10M_\odot$. For objects of mass $0.4M_\odot$ the 95% CL limit is 8%, in conflict with the suggestion by the MACHO collaboration (Alcock *et al.* 2000) that between 7% and 50% of the halo is made up of such objects. The EROS-2 search for microlensing of Galactic Bulge clump giants yielded 120 events (Hamadache *et al.* 2006) giving a Galactic-latitude dependent optical depth of

$$\tau/10^{-6} = (1.62 \pm 0.23)\exp[-a(|b| - 3^\circ)] \,, \quad (1)$$

with

$$a = (0.43 \pm 0.16)\ \mathrm{deg}^{-1} \,. \quad (2)$$

This optical depth agrees with Galactic models (Evans & Belokurov 2002 ; Bissantz *et al.* 1997) and with the results of the MACHO (Popowski *et al.* 2005) and Ogle-II (Sumi *et al.* 2006) collaborations. The duration distribution of the events discovered by the three collaborations have been recently analyzed by Calchi Novati *et al.* 2008 to constrain the Galactic Bulge Initial Mass Function.

Our team has devoted about 15% of the observing time during 7 seasons to the search for microlensing events towards the Galactic Spiral Arms (GSA), as far as 55 degrees in longitude away from the Galactic center. In our previous publications (Derue *et al.* 1999, Derue *et al.* 2001, hereafter referred as papers I and II) describing the detection of respectively 3 and 7 events, our attention was called on a possible optical depth asymmetry, accompanied by an asymmetric event dynamics with respect to the Galactic center. This marginal effect (a 9% probability to be accidental) could be interpreted as an indication of a long Galactic bar within the bulge. Its investigation required a significant increase in the number of events.

In addition to the observing time increase (by more than a factor 2), we improved our catalog of monitored stars by increasing the limiting magnitude as well as by recovering some fields and sub-fields that were not analyzed previously. These improvements allowed us to recover another factor $\sim$ 1.5 in sensitivity. Moreover the discrimination power for microlensing event identification has been significantly improved, partly because the light curves are longer and thus provide a better rejection of recurrent variable objects.

A specific difficulty in the analysis of the spiral arms survey comes from the poor knownledge of the source distance distribution; in contrast with the LMC, the SMC and the Galactic center red giant clump, the monitored sources in the Galactic disk span a wide range of distances (±5 kpc according to preliminary studies, see Sect. 6.4.2). Their mean distance is also uncertain and has been estimated to be $7 \pm 1\ kpc$ (Derue 1999b). We define in this paper the notion of "catalog optical depth" (Sect. 9) and provide all the necessary data to test Galactic models.

2. Microlensing basics

Gravitational microlensing (Paczyński 1986) occurs when a massive compact object passes close enough to the line of sight of a star, temporarily magnifying the received light. In the approximation of a single point-like object acting as a deflector on a single point-like source, the total magnification of the source luminosity at a given time t is the sum of the contributions of two images, given by

$$A(t) = \frac{u(t)^2 + 2}{u(t)\sqrt{u(t)^2 + 4}} \,, \quad (3)$$

where $u(t)$ is the distance of the deflecting object to the undeflected line of sight, expressed in units of the "Einstein Radius" R_E:

$$R_E = \sqrt{\frac{4GM}{c^2} Lx(1-x)} \,, \quad (4)$$
$$\simeq 4.54\ A.U. \times \left[\frac{M}{M_\odot}\right]^{\frac{1}{2}} \times \left[\frac{L}{10\ kpc}\right]^{\frac{1}{2}} \times \frac{[x(1-x)]^{\frac{1}{2}}}{0.5}.$$

Here G is the Newtonian gravitational constant, L is the distance of the observer to the source and xL is its distance to the deflector of mass M. The motion of the deflector relative to the line of sight makes the magnification vary with time. Assuming a deflector moving at a constant relative transverse speed V_T, reaching its minimum distance u_0 (impact parameter) to the undeflected line of sight at time t_0, $u(t)$ is given by

$$u(t) = \sqrt{u_0^2 + ((t - t_0)/t_E)^2}, \quad (5)$$

where $t_E = \frac{R_E}{V_T}$, the "lensing time scale", is the only measurable parameter bringing useful information on the lens configuration in the approximation of simple microlensing:

$$t_E(days) = 79. \left[\frac{V_T}{100\ km/s}\right]^{-1} \left[\frac{M}{M_\odot}\right]^{\frac{1}{2}} \left[\frac{L}{10\ kpc}\right]^{\frac{1}{2}} \frac{[x(1-x)]^{\frac{1}{2}}}{0.5} \,. \quad (6)$$

This simple microlensing description can be broken in many different ways : double lens (Mao & Stefano 1995), extended source, deviations from a uniform motion due either to the rotation of the Earth around the Sun (parallax effect)(Gould 1992, Hardy & Walker 1995), or to the orbital motion of the source around the center-of-mass of a multiple system, or to a similar motion of the deflector (see for example Möllerach & Roulet 2002).

The optical depth τ towards a particular set of target stars is defined as the average probability for the line of sight to intercept the Einstein disk of a deflector (magnification $A > 1.34$). This probability is independent of the deflector mass function, since the surface of the Einstein disk is proportional to the deflector's mass. When the target consists of a population of stars, the *measured* optical depth is obtained from

$$\tau = \frac{1}{N_{obs}\Delta T_{obs}} \frac{\pi}{2} \sum_{events} \frac{t_E}{\epsilon(t_E)}, \quad (7)$$

where N_{obs} is the number of monitored stars; ΔT_{obs} is the duration of the observing period; $\epsilon(t_E)$ is the average detection efficiency of microlensing events with a time scale t_E, defined as the ratio of detected events to the number of events with $u_0 < 1$ whose magnification reaches its maximum during the observing period. Similarly, the event rate corrected for the detection efficiency is

$$\Gamma = \frac{1}{N_{obs}\Delta T_{obs}} \times \sum_{events} \frac{1}{\epsilon(t_E)}. \quad (8)$$

3. Experimental setup and observations

The telescope, the camera and the observations, as well as the operations and data reduction are described in paper I and references therein. The star population locations and the amount of data collected towards the 29 fields that have been monitored in four different regions (β Sct, γ Sct, γ Nor and θ Mus) are given in

Fig. 1 and table 1. Taking into account the dead zones, the lower efficiency sectors of our CCDs and the blind zones around the brightest stars, we estimate that 75 ± 4% of the total CCD area (0.95 deg^2) was effectively sensitive. This number was obtained by estimating the excess of 10×10 pixel domains ($6'' \times 6''$) containing zero star, with respect to the number of void domains expected from the Poissonian distribution of the stellar number density. It is in agreement with the ratio between the total number of detected stars (summed over all fields) and the number extrapolated from the stellar density observed in the CCD best zones. We took exposures of 120 s towards β Sct, γ Sct and γ Nor and 180 s towards θ Mus. The observations span a period of $\Delta T_{obs} = 2325\ days$, starting July 1996 and ending October 2002; 369 measurements per field were obtained on average in each of the R_{EROS} and B_{EROS} bands. Our fields were calibrated using the DENIS catalog (Epchtein *et al.* 1999) and the calibration was checked with the OGLE-II catalog (Udalski *et al.* 2000b). We found that R_{EROS} and B_{EROS} bands are related to the Cousins I and Johnson V magnitudes through the following color equations, to a precision of ∼ 0.1 mag:

$$R_{EROS} = I_C\ , \quad B_{EROS} = V_J - 0.4(V_J - I_C). \tag{9}$$

Figure 2 shows the observation time span and the average sampling for the four different directions.

Table 1. Characteristics of the 29 fields which were monitored in the EROS spiral arm program: Locations of the field centers, average sampling (number of photometric measurements per light curve and per color) and number of stars monitored for each field. The observing time was $\Delta T_{obs} = 2325\ days$. The total numbers of observed stars towards γ Nor and θ Mus are smaller than the sum of the numbers given for each field because of some overlap between contiguous fields. The total fields of view (f.o.v.) are the areas effectively monitored (0.71 deg^2 per field, see text), corrected for the overlap between fields.

Field	α° (J2000)	δ° (J2000)	b°	l°	N_{meas}	N_{obs} (10^6)
β Sct **Exposure** = **120s**. **f.o.v.** = **4.3 deg^2**.					268	3.00
bs300	280.8417	-7.6814	-1.75	25.20	269	0.48
bs301	280.8625	-6.2283	-1.11	26.51	266	0.47
bs302	281.5667	-7.3792	-2.25	26.80	272	0.50
bs303	281.5833	-5.9264	-1.60	27.09	261	0.47
bs304	282.3375	-6.7642	-2.70	26.71	269	0.52
bs305	283.1083	-6.5956	-3.26	27.19	271	0.54
γ Sct **Exposure** = **120s**. **f.o.v.** = **3.6 deg^2**.					277	2.38
gs200	277.0125	-14.8517	-1.64	17.72	282	0.47
gs201	277.8125	-14.2439	-2.12	18.00	266	0.49
gs202	277.8875	-12.8147	-1.52	19.30	291	0.49
gs203	278.5917	-14.5275	-2.92	18.09	281	0.46
gs204	278.6167	-13.0753	-2.28	19.40	267	0.47
γ Nor **Exposure** = **120s**. **f.o.v.** = **8.4 deg^2**.					454	5.24
gn400	242.4375	-53.1175	-1.17	330.49	496	0.42
gn401	244.5917	-51.7453	-0.99	332.04	475	0.41
gn402	243.7375	-53.0764	-1.59	330.74	463	0.45
gn403	245.6167	-52.1056	-1.69	332.24	420	0.42
gn404	244.7875	-53.4439	-2.29	330.94	435	0.43
gn405	246.7167	-52.3506	-2.35	332.54	445	0.44
gn406	245.9750	-53.7314	-2.99	331.23	443	0.46
gn407	247.8792	-52.4789	-2.95	332.93	443	0.47
gn408	247.1750	-53.8661	-3.60	331.63	453	0.47
gn409	243.9625	-54.8125	-2.86	329.82	482	0.47
gn410	245.1250	-55.0717	-3.59	329.93	443	0.46
gn411	242.4042	-55.1686	-2.54	328.78	449	0.48
θ Mus **Exposure** = **180s**. **f.o.v.** = **3.8 deg^2**.					375	2.28
tm500	201.7667	-63.0383	-0.47	306.98	391	0.44
tm501	202.8250	-63.5781	-1.07	307.37	355	0.44
tm502	203.7167	-64.1750	-1.72	307.66	376	0.47
tm503	200.9917	-64.9978	-2.36	306.38	375	0.36
tm504	198.0500	-64.1136	-1.35	305.22	392	0.43
tm505	199.0625	-64.6806	-1.96	305.60	360	0.43
					Total	12.9

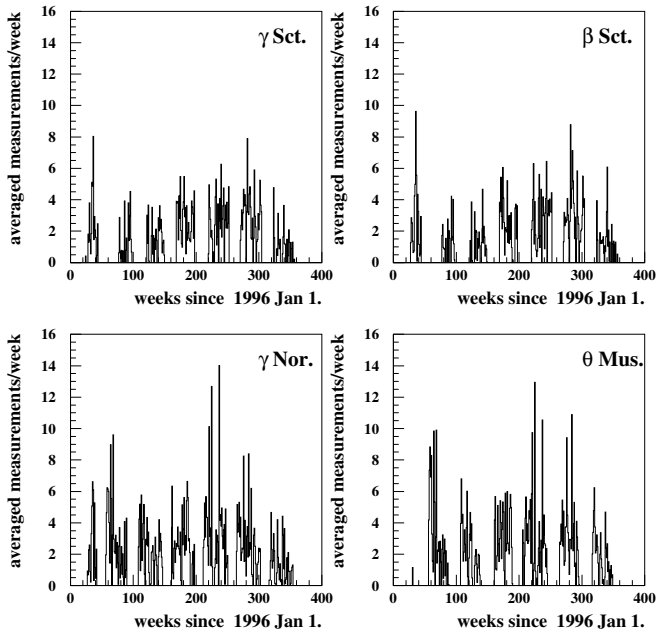

Fig. 2. Time sampling for each monitored direction: weekly average number of measurements per star since January 1rst, 1996.

4. The catalogs

The catalogs of monitored stars have been produced following the procedure described in papers I and II, based on the PEIDA photometric software (Ansari 1996). All objects are well identified in both colors and unambiguously associated between these two colors. We have removed objects that suffer from a strong contamination by a nearby bright star; the contribution to the background flux from such a nearby star at the position of the object should not exceed 150% of its peak flux.

The seven season data set contains 12.9 million objects measured in the two colors: 3.0 towards β Sct, 2.4 towards γ Sct, 5.2 towards γ Nor and 2.3 towards θ Mus. The number of monitored stars was increased by ∼ 50% since the analysis of papers I and II, by producing a richer catalog from a wider choice of good quality images than available before. We were also able to solve some technical problems that prevented us from producing the catalog for some fields (Tisserand 2004, Rahal 2003). The recovered stars are mainly faint stars with a comparatively low microlensing sensitivity.

4.1. Completeness, blending

We have compared a subset of the gs201 EROS field catalog (Fig. 3a) with the catalog extracted from the deeper HST-WFPC2 (Wide Field Planetary Camera 2) images (Fig. 3b) named U6FQ1102B (exposure 210s with filter F606W) and U6FQ1104B (exposure 126s with filter F814W), centered at ($\alpha = 277.6281°$, $\delta = -14.4823°$) or ($b = 17.689814°, l = -2.039549°$), obtained from the HST archive (HST 2002). We detected 3518 stars in both colors in the HST images corresponding to the EROS monitored field; we systematically tried to associate these stars with an EROS object within 1 arcsec. All of the 869 EROS-objects properly identified as stars in the field

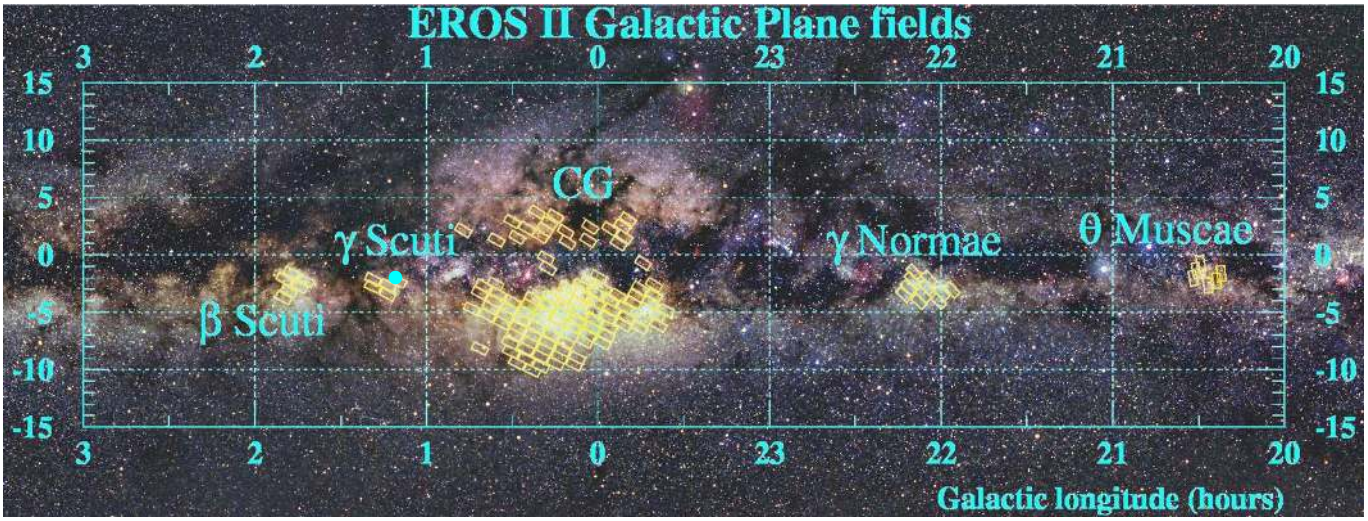

Fig. 1. The Galactic plane fields (Galactic coordinates) monitored by EROS superimposed on the image of the Milky-way. The locations of our fields towards the spiral arms, as well as our Galactic bulge fields (not discussed in this paper) are shown. The large blue dot towards γ Sct indicates the position of the HST field used to estimate our star detection efficiency (see text). North is up, East is left.

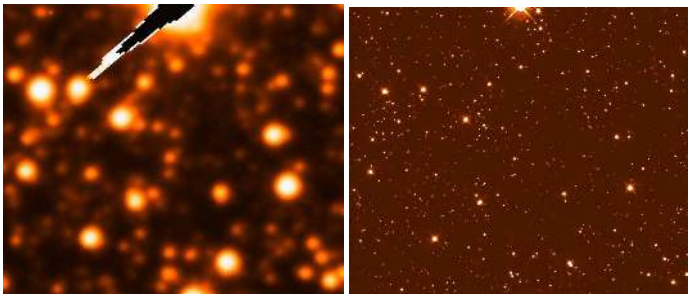

Fig. 3. (a) The R_{EROS} composite image (used to detect the cataloged stars) and (b) the U6FQ1104B-HST image of the same sub-field towards gs201.

were associated with one or more HST star, allowing a study of the blending and of the detection efficiency as a function of the magnitude. We found that 56% of the EROS objects are blends with more than one HST-star within 1 arcsec distance. In this case the brightest HST-star accounts for an average of 72% of the B_{EROS} flux of the EROS object. These numbers vary with the EROS object magnitude as follows:

B_{EROS}	**15-17**	**17-19**	**19-21**
fraction of blended EROS-objects	70%	59%	54%
contribution of main HST star	88%	77%	68%

The comparison of these numbers with the ones found from a similar study of a LMC dense field (Tisserand *et al.* 2007) indicates that EROS cataloged objects towards gs201 are on average less blended than the objects found towards dense regions of LMC. Such blending could affect the microlensing optical depth determination, as discussed in detail for SMC fields in (Afonso *et al.* 2003), and the distribution of the lensing time scale t_E (Rahvar 2004; Bennett 2005). The average densities of the EROS catalogs are similar towards the SMC and the spiral arms; therefore one should expect differences in blending only if there is a difference between the spatial repartitions of the 2 stellar populations. Since our studies of HST images have shown that the spiral arm stars are less blended than the LMC stars, and considering the similarity between the SMC and the LMC populations, we conclude that blending should have less impact towards the spiral arms than towards the SMC. Therefore, to be conservative, we will use the estimates of (Afonso *et al.* 2003) as upper limits on the optical depth systematic uncertainties in Section 7.2.

From the HST-EROS star association, we have extracted our detection efficiencies as a function of the B_{EROS} stellar magnitudes (see figure 4). As F814W and F606W HST-WFPC2 filters are respectively very close to our R_{EROS} and B_{EROS} bands, we could directly measure detection efficiencies for HST objects. We found that every HST star that is detected in the EROS images (i.e. that is located within 1 arcsec of an EROS object) in the B_{EROS} band is automatically detected in the R_{EROS} band (the reverse is false). This is due to the different limit magnitudes of the B_{EROS} and R_{EROS} templates. Therefore the efficiency to detect a HST star in EROS is the probability for that star to be found in the B_{EROS} band. The color-magnitude diagrams of Fig. 5 show that the diagonal delimitations of the populations in the bottom right sector follow a $B_{EROS} = constant$ line, thus confirming that the detection threshold is set by B_{EROS}. We estimate the efficiency within the active region of the CCD-array, corresponding to the effective field of 0.71 deg^2 for the full mosaic. We provide in Fig. 4 the probability for a HST star to be the main contributor of an EROS object. A star can also have a minor contribution to the flux of an EROS object, as a result of blending; we show also the probability for HST stars to contribute to an EROS object (even if not as the main contributor).

4.2. The color-magnitude diagram

Figure 5 gives the color-magnitude diagrams $n_{eros}(I, V-I)$ of our catalogs[1]. The global pattern of these diagrams follows the expected magnitude versus color lines resulting from the light absorption of a distance-distributed stellar population. Two parallel features are visible, with very different densities.

[1] 2D-tables of these diagrams can be found on the Web-site: http://users.lal.in2p3.fr/moniez/

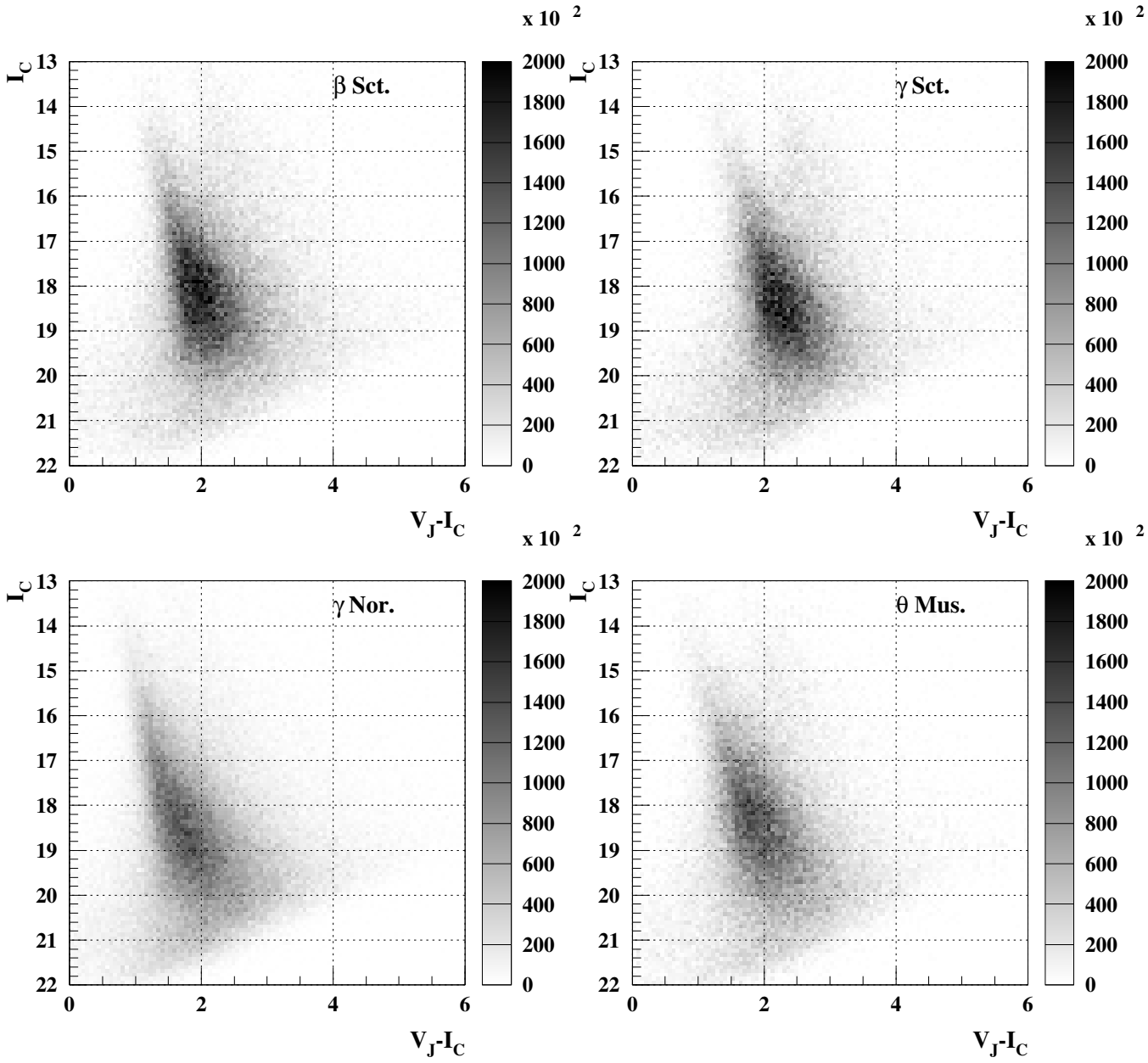

Fig. 5. Color-magnitude diagrams $n_{eros}(I, V-I)$ of our catalogs towards the 4 monitored directions. The grey scale gives the number density of stars per square degree, per unit of magnitude and per unit of color index.

We were able to qualitatively reproduce these features with a (simple) simulated catalog (Fig. 21). The color-magnitude diagram of this synthesized catalog shows two parallel features due to the main sequence and the red giant clump, that are similar to the ones observed in the data. Without spectroscopic data or a more detailed simulation, it is not possible to go further than this qualitative comparison for the interpretation of the observed color-magnitude diagrams.

4.3. Photometric precision

To complete the description of our observations, Fig. 6 gives the average point-to-point photometric dispersion along the light-curves as a function of the magnitude I_C.

5. The search for lensed stars

Our microlensing event detection scheme is the same as the one described in papers I and II. In the following, we will outline the few specificities that arise because of analysis improvements, specific seasonal conditions or particular problems, and because

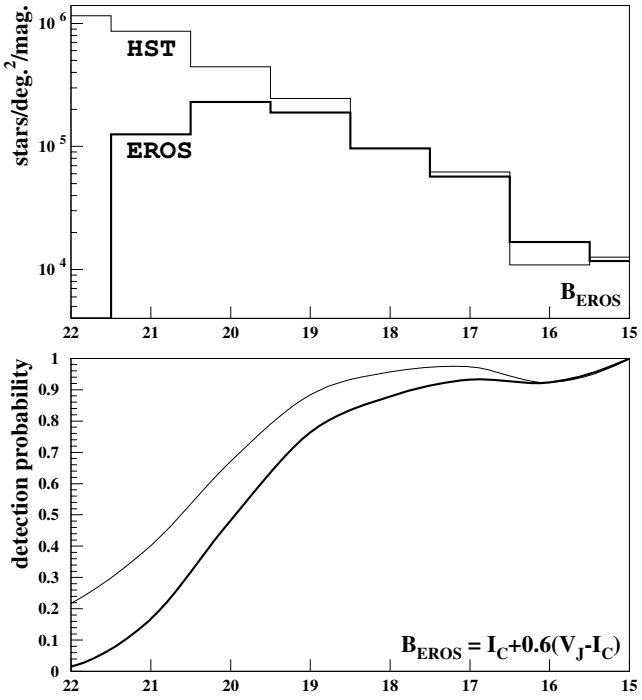

Fig. 4. - Top panel: The EROS (thick line) and HST (thin line) $B_{EROS} = I_C + 0.6(V_J - I_C)$ magnitude distributions of the identified objects in a sub-field of gs201. Objects brighter than $B_{EROS} = 16$ are all identified in both images, but their magnitudes are systematically overestimated by our photometry in the HST image, explaining the apparent deficiency of bright HST objects.
- Lower panel: The thin line shows the probability for an HST star to contribute to an EROS object, i.e. to be closer than 1 arcsec from such an object versus $B_{EROS} = I_C + 0.6(V_J - I_C)$.
The thick line gives the probability for an HST star to be the main contributor to the flux of an EROS object found within 1 arcsec.

of the fact that the time baseline is twice to three times longer than in our previous publications.

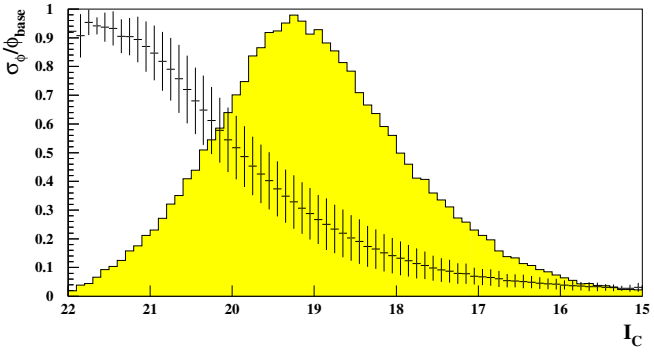

Fig. 6. Average photometric point-to-point precision along the light-curves versus I_C. The vertical bars show the dispersion of this precision in our source sample. The histogram shows the magnitude distribution of the full catalog (average over 4 directions).

5.1. Prefiltering

We used the same non specific prefiltering described in paper II, and preselected the most variable light curves satisfying at least one of the following criteria:

- The strongest fluctuation along the light curve (a series of consecutive flux measurements that lie below or above the "base flux", i.e. the average flux calculated in time regions devoid of significant fluctuations) has a small probability (typically smaller than 10^{-10}) to happen for a stable star, assuming Gaussian errors;
- The dispersion of the flux measurements is significantly larger than expected from the photometric precision;
- The distribution of the deviations with respect to the base flux is incompatible with the distribution expected from the measurements of a stable source with Gaussian errors (using the Kolmogorov-Smirnov test).

The thresholds of these three criteria have been tuned to select a total of $\sim 20\%$ of the light curves. After this prefiltering, 2446843 light curves are entering the more discriminating analysis described below. We also included a randomly selected set of light curves ($\sim 2\%$) to produce unbiased color-magnitude diagrams and for our efficiency calculation (Sect. 7.1). Furthermore, we have corrected the photometric measurements presenting a significant correlation between the flux and the seeing in a way that is described in (Tisserand 2004).

5.2. Filtering

- As in paper II, we first searched for bumps in each light curve. A bump is defined as a series of consecutive flux measurements that starts with a positive fluctuation of more than one standard deviation ($+1\sigma$) from the base flux, ends when 3 consecutive measurements lie below 1σ from the base flux and contains at least four measurements deviating by more than $+1\sigma$. We characterize such a bump by the parameter $Q = -log_{10}(P)$ where P is the probability that the bump be due to an accidental occurrence in a stable star light curve, assuming Gaussian errors. We select the light curves whose most significant fluctuation (bump 1) is positive in both colors.
- Then we require the time overlap between the main bumps in each color to be at least 10% of the combined time intervals of the two bumps.
- To reject most of the periodic or irregular variable stars, we remove those light curves that have a second bump (bump 2, *positive or negative*) with $Q_2 > Q_1/2$ in one color.

After this filtering, the 1097 remaining light curves can be fitted assuming the simplest microlensing hypothesis, *i.e.* a point-like source and a point-like deflector with a constant speed.

5.3. Candidate selection

The observed flux versus time data $\Phi_{obs}(t_i)$ is fitted with the expression $\Phi(t) = \Phi_{base} \times A(t)$, where Φ_{base} is the unmagnified flux and $A(t)$ is given by expression (3). The candidate selection is based on the fit quality (χ^2) and on variables obtained from the Φ_{base}, t_0, t_E and u_0 fitted parameters. We apply the following criteria, tuned to select not only the "simple" microlensing events, but also events that are affected by small deviations due to parallax, source extension, binary lens effects... mentioned in Sect. 2. The efficiency to detect caustics should be very limited

with this set of cuts, but none was found from a systematic visual inspection of the 1097 light curves.

– **C1. Minimum observation of the unmagnified epoch :** We first reduce the background due to instrumental effects and to field crowding problems by selecting light curves that are sufficiently sampled both during the unmagnified and the magnified stages. For this purpose we define the "high" magnification epoch (called *peak*, labeled "$u < 2$") as the period of time during which the fitted magnification A is above 1.06, associated to an impact parameter $u < 2$. The complementary "low" magnification epochs, during which $A < 1.06$, are labeled $''base''$. We require that

$$\Delta T_{obs} - \Delta T_{u<2} > 600\, days, \tag{10}$$

where $\Delta T_{obs} = 2325.\, days$ is the observation duration, and $\Delta T_{u<2}$ is the duration of the "high" magnification epoch.

– **C2. Sampling during the magnified epoch :** We also require that the interval between the peak magnification time t_0 and the nearest measurement is smaller than $0.4 \times \Delta T_{u<2}$.
– **C3. Goodness of a simple microlensing fit :** To ensure the fit quality, we require $\chi^2_{ml}/N_{dof} < 1.8$ separately for both colors, where χ^2_{ml} and the number of degrees of freedom N_{dof} are obtained from the full light-curve.
– **C4. Impact parameter :** We also require that the fitted impact parameter u_0 be less than 1 for both colors.
– **C5. Stability of the unmagnified object :** One important feature of a microlensing light curve is its stability during the low magnification epochs, except for the rare configurations of microlensed variable stars. We reject light curves with

$$\frac{\chi^2_{base}(R) + \chi^2_{base}(B)}{N_{dof}(R) + N_{dof}(B)} > 8, \tag{11}$$

where the χ^2_{base} and N_{dof} values correspond to the measurements obtained during the low magnification epochs.
– **C6. Improvement brought by the microlensing fit compared to a constant fit :** We use the same $\Delta\chi^2$ variables as in paper II to select light curves for which a simple microlensing fit is significantly better than a constant value fit:

$$\Delta\chi^2_{B,R} = \frac{\chi^2_{cst} - \chi^2_{ml}}{\chi^2_{ml}/N_{dof}} \frac{1}{\sqrt{2N_{dof}}}\Big|_{B,R}. \tag{12}$$

We select light curves with $\Delta\chi^2_B + \Delta\chi^2_R > 60$.
– **C7. Overlap in the two colors :** Defining $\Delta T_{u<1}$ as the time interval during which the fitted magnification is larger than 1.34 ($u < 1$), we require a minimum overlap between the time intervals found in the two colors:

$$\frac{\Delta T_{u<1}(R) \cap \Delta T_{u<1}(B)}{\Delta T_{u<1}(R) \cup \Delta T_{u<1}(B)} > 0.4\,. \tag{13}$$

This loose requirement on the simultaneity of the magnifications in the two colors allows one to keep a good sensitivity to "complex" microlensing events; for example, this cut tolerates some difference between the fitted impact parameters obtained in the two colors (which may occur in the case of strong blending).

The number of microlensing candidates so far is 27 including an uncertain one, labeled GSA-u1 (see below). The I_C magnitudes and $(V_J - I_C)$ colors versus u_0 of these candidates are shown in Fig. 7 together with a sample of points representing the population obtained after selection of simulated events as explained in Sect. 7.1. One clearly sees how the maximal source magnitude required for detection decreases when the impact parameter increases. Annex A shows the light-curves and the finding charts of the 27 candidates, and table 2 gives their characteristics. The finding charts are obtained from the reference images used for the production of the catalogs.

5.4. Non standard microlensing events

Some of our candidates are significantly better fitted with microlensing curves resulting from complex configurations than with the basic point-like source, point-like deflector with a constant-speed microlensing curve. The refinements that have been introduced in these cases are:

– The blending of the lensed source with a nearby, unresolved object. In that case, the light-curve $\Phi_{obs}(t_i)$ has to be fitted by the following expression

$$\Phi(t) = C \times \Phi_{base} \times A(t) + (1 - C) \times \Phi_{base}\,, \tag{14}$$

where C depends on the color. In supplement to the standard fit, this fit provides the C_R and C_B parameters, where C=(base flux of magnified component)/(total base flux). In the notes of table 2, we give the magnitudes and colors of the microlensed components that take into account the color equations (9).
– Parallax. Due to the rotation of the Earth around the Sun, the apparent trajectory of the deflector with respect to the line of sight is a cycloid instead of a straight line. For some configurations (a nearby deflector and an event that lasts a few months), the resulting magnification versus time curve may be affected by this parallax effect (Gould 1992, Hardy & Walker 1995). The specific parameters that can be fitted in this case are the Einstein radius $\tilde{r}_E$ and an orientation angle, both projected on the observer's plane which is orthogonal to the line of sight.
– "Xallarap". This effect is due to the rotation of the source around the center-of-mass of a multiple system. In this case, the light-curve exhibits modulations with a characteristic time given by the period of the source rotation (Derue *et al.* 1999, Möllerach & Roulet 2002). Assuming a circular orbit, the extra-parameters to be fitted or estimated are the orbital period P, the luminosity ratio of the lensed object to the multiple system, and the projected orbit radius in the deflector's plane $\rho = ax/R_E$, where a is the orbit radius and $x = D_{lens}/D_{source}$.

In some cases, the values obtained for t_E with the basic fit and the refined one may differ considerably. For time duration studies and for optical depth calculations, we use the t_E values given by the best fit. But as far as efficiency values are concerned, we must use those obtained with the standard fit since they are the ones that enter the selection procedure.

6. The microlensing candidates

6.1. General features

In order to quantify the relevance of the interpretation of the 27 selected objects as microlensing events, we define two variables as follows:

Table 2. Characteristics of the 27 microlensing candidates. For those events that have a better fit than the point-like point-source constant speed microlensing fit (the so-called standard fit), we also provide the standard fit parameters.
- Names in bold type correspond to events selected for the optical depth and duration analysis (with $u_0 < 0.7$).
- I_C $(V_J - I_C)$ are the fitted unmagnified magnitudes of the lensed object (including the contribution of a possible blend).
- t_0 is the time of maximum magnification, given in HJD-2,450,000.
- t_E is the Einstein disk crossing time, in days.
- u_0 is the dimensionless impact parameter.
- χ^2/dof corresponds to the best microlensing fit.
- τ is the individual contribution of each event to the optical depth towards the corresponding target. In the case of "non standard" events, we use the t_E value obtained from the best (non standard) fit and the efficiency evaluated at t_E of the standard fit (see text) for the calculation of τ.

candidate	field	α°	δ° (J2000)	I_C $(V_J - I_C)$	t_0(days)	t_E(days)	u_0	$\chi^2/d.o.f$	$\tau(10^{-6})$	note
γ Sct										
GSA1	200	277.2888	-14.2528	18.3 (3.1)	301.2± 0.1	64.0± 1.2	.043±.0010	299.7/435	0.146	
GSA8	200	276.8042	-15.0311	16.6 (3.7)	996.9± 0.1	40.6± 1.0	.145±.003	981./533	0.114	(1)
			Standard fit parameters:		993.0± 0.1	35.2± 0.7	.155±.002	1400./535		
GSA9	200	277.1750	-15.1644	18.8 (2.8)	1760.3± 1.7	57.9± 3.6	.482±.0158	262.9/565	0.142	
GSA10	200	277.2813	-14.8931	18.1 (2.3)	1806.1± 0.8	24.6± 1.3	.574±.0179	237.9/596	0.081	
GSA11	201	278.1650	-14.1094	18.8 (2.5)	1725.3± 0.4	44.3± 1.4	.187±.0049	367.2/558	0.116	
GSA12	203	278.5875	-13.9794	17.1 (1.8)	1378.6± 0.2	50.1± 0.7	.225±.0030	89.3/359	0.123	
GSA13	203	278.9404	-14.5803	17.2 (1.9)	313.9± 1.2	37.2± 2.1	.898±.0153	244.9/617	-	
GSA14	204	278.4388	-12.8678	16.7 (2.2)	1637.7± 3.4	68.4± 3.7	.785±.0097	421.2/392	-	(2)
β Sct										
GSA15	301	281.0654	-6.0339	18.3 (3.5)	1399.8± 1.4	72.2± 2.8	.337±.0126	212.2/411	0.110	edge
GSA16	301	280.7646	-6.7583	16.4 (3.1)	1997.0± 3.2	60.6± 4.0	.796±.0141	341.8/361	-	
GSA17	302	281.3950	-7.8867	16.4 (1.7)	1947.2± 3.8	50.0± 2.4	.532±.1079	156.9/400	0.096	
GSA18	304	282.2879	-7.2500	16.1 (2.1)	1718.7± 0.1	55.0± 2.0	.137±.0009	133./514	0.098	(3)
			Standard fit parameters:		1718.4± 0.1	58.0± 0.3	.137±.0009	155.6/516		
γ Nor										
GSA2	400	242.9592	-52.9464	18.6 (2.3)	534.4± 0.2	98.3± 0.9	.342±.002	973.4/934	0.059	(4)
			Standard fit parameters:		533.6± 0.5	137.8± 2.6	.233±.0029	1196.5/937		
GSA19	401	244.1379	-52.0272	15.5 (5.1)	2367.7± 1.3	90.4± 3.0	.043±.025	893./880	0.063	(5)
			Standard fit parameters:		2373.5± 0.1	93.1± 0.7	.022±.007	1388.5/888		
GSA20	402	243.7758	-52.9700	16.4 (1.3)	2465.5± 1.0	40.± 5.0	.72±.02	414./696	0.039	(6)
			Standard fit parameters:		2487.1± 0.3	46.3± 0.7	.565±.0050	712.4/698		
GSA21	404	244.3063	-53.1100	16.8 (2.7)	1587.3± .03	74.± 3.0	.0142±.0008	259./565	0.077	(7)
			Standard fit parameters:		1587.2± .03	39.1± 0.2	.037±.0007	1884.4/567		
GSA22	404	244.4263	-54.0508	18.4 (2.0)	2182.4± 0.2	26.6± 1.1	.048±.0180	429.5/742	0.031	
GSA23	404	245.1208	-53.9825	18.3 (1.7)	1573.8± 3.8	78.5± 5.7	.542±.0152	522.3/784	0.062	corner
GSA24	406	246.5442	-54.0394	18.0 (1.9)	2002.5± 1.4	55.5± 2.6	.720±.0158	579.4/786	-	
GSA25	408	247.6917	-53.9281	21.1 (1.4)	850.9± .03	67.6± 2.9	.003±.0001	876.2/771	0.057	(8)
GSA3	409	244.1129	-54.6303	17.7 (1.4)	696.0± 2.0	60.4± 3.0	.615±.0102	606.7/1090	0.051	
GSA26	411	241.8729	-55.3814	17.8 (2.2)	1642.1± 0.3	23.2± 0.8	.504±.0138	441.5/759	0.030	
GSA27	411	242.4846	-55.2292	18.3 (1.7)	2193.8± 0.1	6.8± 0.4	.210±.0068	433.6/831	0.022	
θ Mus										
GSA28	501	202.2838	-64.2750	19.3 (3.7)	1992.2± 0.4	205.± 20.0	.029±.004	717/499	0.431	(9)
			Standard fit parameters:		1992.0± 0.4	87.3± 3.0	.094±.0046	868.5/500		
GSA29	502	204.0683	-63.7117	19.3 (2.5)	1229.7± 0.3	74.2± 2.7	.082±.0042	161.7/354	0.166	
GSA30	505	199.2942	-64.2592	16.5 (2.7)	2396.9± 0.1	12.4± 0.2	.062±.0023	792.0/856	0.073	
Uncertain candidate										
GSAu1	202	278.0371	-13.2851	18.1 (2.9)	1695.8± 6.9	409.3±20.9	.708±.0155	426.9/613		

Notes: (1) GSA8: Blended; $C_R = 1.00 \pm 0.03$, $C_B = 0.68 \pm 0.02$; lensed star has I_C^* $(V_J^* - I_C^*) = 16.6$ (4.4). **(2) GSA14**: Light-curve exhibits typical features of a binary lens system. Given the small number of measurements with significant magnification, no reliable analysis of the shape can be performed. **(3) GSA18**: Parallax; projected Einstein radius in the solar plane $\tilde{r}_E = 12.5 \pm 7.0 AU$. **(4) GSA2**: Described in paper I. Found at that time as the first candidate for a binary lensed source (Xallarap). **(5) GSA19**: Xallarap and blend; the best fit is performed ignoring the 3 most magnified measurements, that are affected by the non-linearity of the CCD. $C_R = 1.$, $C_B = 0.160 \pm 0.013$; lensed star has I_C^* $(V_J^* - I_C^*) = 15.5$ (8.4). The light-curve distortion could be due to the face-on circular orbiting of the source around the center-of-mass of a system including a non luminous object, with period $P_0 = 294. \pm 47.$ *days*, and with a projected orbit radius of $\rho = ax/R_E = 0.081 \pm 0.023$, where a is the orbit radius and $x = D_{lens}/D_{source}$. See also text. **(6) GSA20**: Parallax; $\tilde{r}_E = 0.94 \pm 0.07 AU$. **(7) GSA21**: Blended; $C_R = 0.53 \pm 0.02$, $C_B = 0.34 \pm 0.02$; lensed star has I_C^* $(V_J^* - I_C^*) = 17.5$ (3.5). **(8) GSA25**: An improbable configuration, but a genuine one (very small u_0 on a very faint star). **(9) GSA28**: Blended; $C_R = 0.30 \pm 0.03$, $C_B = 1$; lensed star has I_C^* $(V_J^* - I_C^*) = 20.6$ (1.5). The χ^2/dof of the fit is affected by an underestimate of the errors due to bright neighboring stars.

– Ideally, the goodness of the microlensing fit should be uniform throughout the observation duration. Here we use fits made separately in the two colors. Let $\chi^2_{u<2}$ and $n_{u<2}$ be the microlensing fit χ^2 and the number of degrees of freedom, restricted to the high magnification epoch ($u < 2$, $A > 1.06$, see Sect. 5.3). Let χ^2_{base} and n_{base} be the complementary vari-

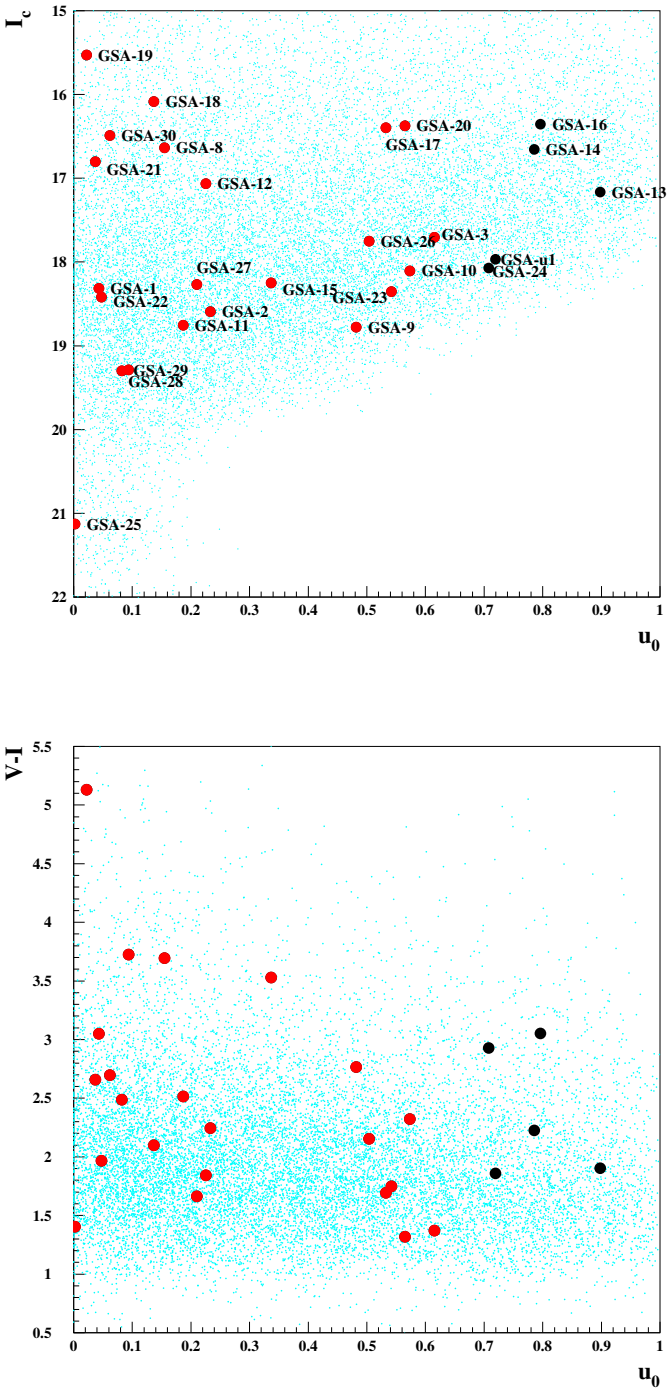

Fig. 7. Top panel: I_C versus fitted u_0 for the 27 microlensing candidates. Bottom panel: $V_J - I_C$ versus fitted u_0. u_0 is the fitted value assuming a point-like source and a point-like deflector with a constant speed. The red dots (respectively black dots) correspond to events with $u_0 < 0.7$ used for optical depth studies (resp. $0.7 < u_0 < 1.$). The small dots are the simulated events that satisfy the microlensing selection criteria.

ables outside the peak period. The variable

$$\delta_{fit} = \left[\frac{\chi^2_{u<2}(R) + \chi^2_{u<2}(B)}{n_{u<2}(R) + n_{u<2}(B)} - \frac{\chi^2_{base}(R) + \chi^2_{base}(B)}{n_{base}(R) + n_{base}(B)}\right]$$

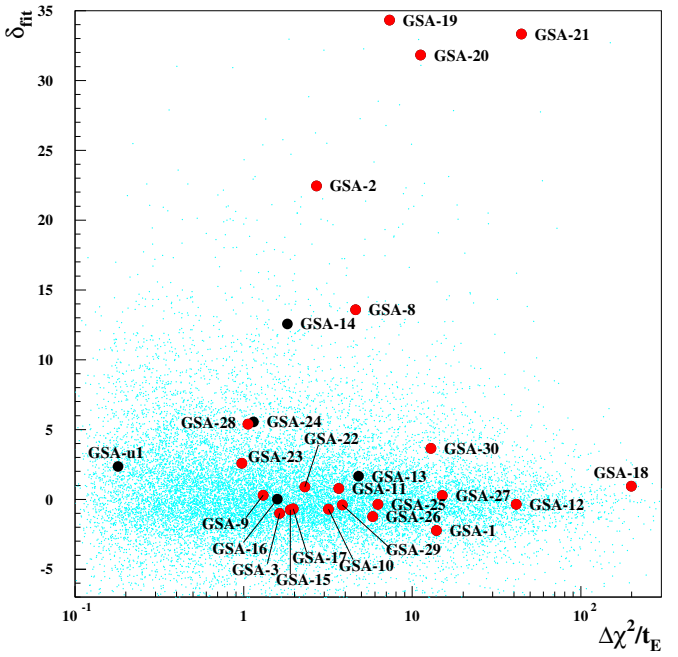

Fig. 8. δ_{fit} versus $(\Delta\chi^2_B + \Delta\chi^2_R)/t_E$ for the microlensing candidates. Red dots correspond to events with fitted $u_0 < 0.7$. The small dots represent the simulated events that satisfy the microlensing selection.

$$\times \left[\frac{1}{n_{u<2}(R) + n_{u<2}(B)} + \frac{1}{n_{base}(R) + n_{base}(B)}\right]^{-\frac{1}{2}} \quad (15)$$

quantifies the difference of the standard fit quality during and outside the microlensing peak, expressed in standard deviations (thanks to the second factor). A negative value of δ_{fit} (< -5) is an indication of a non constant base, and points to a variable star instead of a microlensing event. For non-standard microlensing (parallax, blending...) δ_{fit} will be positive and may be large (> 10), because the fit is expected to be less good in the peak than in the base.

– Many of the EROS instrumental defects —such as bad pixels or diffraction features— have a long lifetime, and last for entire observing seasons. This produces long time scale false candidates. A signal to noise indicator is provided by the ratio $(\Delta\chi^2_B + \Delta\chi^2_R)/(t_E/1\ day)$ where $\Delta\chi^2$ is defined above (criterion C6) and where t_E characterizes the event time scale.

Figure 8 shows the distribution of δ_{fit} versus $(\Delta\chi^2_B + \Delta\chi^2_R)/(t_E/1\ day)$ for the data satisfying the filtering conditions, for the final candidates and for the simulated sample (see Sect. 7.1). Within our final sample, three subgroups are apparent:

– a few (6) selected events have both a large positive δ_{fit} and $(\Delta\chi^2_B + \Delta\chi^2_R)/t_E$. These are events for which a non-standard microlensing fit provides a better interpretation. Each of them is discussed in the remarks of table 2.
– the bulk of our final sample (20) are events with a large $(\Delta\chi^2_B + \Delta\chi^2_R)/t_E$ and δ_{fit} compatible with 0, as expected for standard microlensing events (and as is the case for our simulated sample).
– Event GSA-u1 has a small $(\Delta\chi^2_B + \Delta\chi^2_R)/t_E$. After visual inspection (see Annex A, last event), we cannot exclude a microlensing interpretation, but the long duration and the lack

of a reliable base make it very uncertain, considering the relatively low value of $\Delta\chi^2_B + \Delta\chi^2_R$ (only 73.). The status of this candidate remains pending until further observations over a longer time range can be made. One should keep in mind that confirmed events of this type would give a major contribution to the optical depth (GSAu1 would contribute for $\sim 0.5 \times 10^{-6}$ towards θ Mus).

6.2. Comparison with the EROS 3 year analysis (paper II)

We first checked the coherence between the present results and those of paper II. Three additional candidates (GSA8, 13 and 25) with a maximum occurring during the first three years have been found. GSA13 and GSA25 belong to subfields that were not analyzed in paper II. GSA8 is located at the border of two subfields, and was missed by our previous analysis that did not systematically explore the overlapping regions between subfields.

Four of the 7 candidates, all towards γ Sct, found in paper II are now rejected for the following reasons:

- GSA4 and GSA7 both showed a second fluctuation after the first three years.
- For GSA5, the χ^2 improvement when replacing a constant fit by a microlensing fit is no longer significant enough, due to the low signal to noise ratio that prevails for its light curve during the 7 years of data taking.
- GSA6 was found to have an impact parameter of 0.98 ± 0.04 in paper II. Taking into account the full light curve, the new fitted value is $u_0 = 1.03 \pm 0.07$, now just above our threshold. Incidentally, $\Delta\chi^2$ is also much smaller than our threshold (60), indicating that the previous selection of this event could have been due to a fluctuation.

One notices that these rejected candidates were the low signal/noise ones towards γ Sct. Clearly, 7 years of observations allow a much better noise reduction than 3 years.

6.3. Overlap with other published surveys

A very small region of γ Nor overlaps with the OGLE II microlensing survey (OGLE webpage). No event from this region was reported in the latter survey (Udalski *et al.* 2000a).

A small region of our survey overlaps the MACHO fields (Thomas *et al.* 2005). Amongst the 9 MACHO candidates or alerts found around γ Sct, 3 are located within one of our monitored fields, but have not been selected in our analysis for the following reasons:

- MACHO alert number 302.44928.3523 is too faint to be measured in B_{EROS} and no measurement was made in R_{EROS} within 40 days of the magnification maximum. Nevertheless, an object clearly appears in the B_{EROS} images around the maximum magnification date.
- MACHO alert number 301.45445.840 is too faint to be in the EROS catalog. Furthermore, EROS missed the event as its time of maximum magnification was 106 days before the first EROS observation of the corresponding field.
- MACHO alert number 302.45258.1038 was very close to one of the gaps located between CCDs. Thus many measurements are missing. Our standard procedure does not try to recover complete light-curves in such a case, and the standard light-curve failed our selection process. Nevertheless, we confirm the presence of the bump at the right time, with the maximum magnification occurring during the very first days of the EROS data taking.

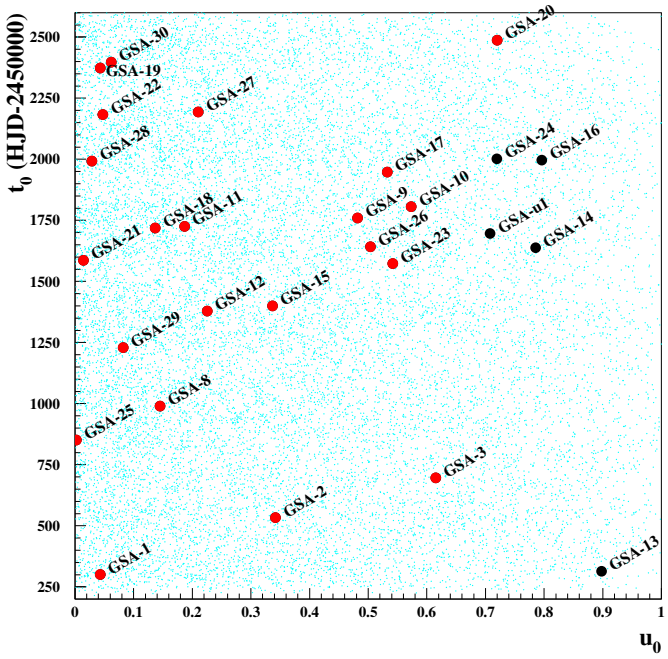

Fig. 9. t_0 versus fitted u_0 for the simulated events satisfying the analysis criteria (small dots) and for the detected candidates (big dots). Red dots correspond to events with fitted $u_0 < 0.7$ ("standard" fit). In the case of complex events, the **best fit** u_0 value is plotted.

6.4. Statistical properties of the candidate parameters

6.4.1. The lens configurations

Microlensing events occur with a flat-distributed impact parameter and minimum approach time. The sample of observed microlensing event (t_0, u_0) configurations should be statistically representative of such a distribution after taking into account our detection efficiencies. This is illustrated in Fig. 9, where simulated events are generated as described in Sect. 7.1.

6.4.2. The microlensed star population

The microlensed star population should also be representative of the monitored population weighted by the microlensing detection efficiencies and by the optical depth that may vary from source to source. As the sources are likely to be distributed along the line of sight, a possible variation of the optical depth with distance must be considered in the data analysis. As the light of a remote source is expected to be more reddened than the light of a close one, the optical depth τ should increase on average with the color index. Figure 10 shows our color-magnitude diagram, weighted by the microlensing efficiencies and *assuming the same optical depth for all stars*. It is directly obtained from the simulated events that satisfy the analysis requirements. The distribution of the observed candidates is less peaked than the simulated one in the low color index region because the most reddened stars are more likely to be lensed. We were able to qualitatively confirm this color bias through the catalog produced with a simple simulation towards γ Sct described in Sect. 9.2, that takes into account the source distance distribution (Fig. 11 left). Fig. 11(right) shows that the color distribution of the

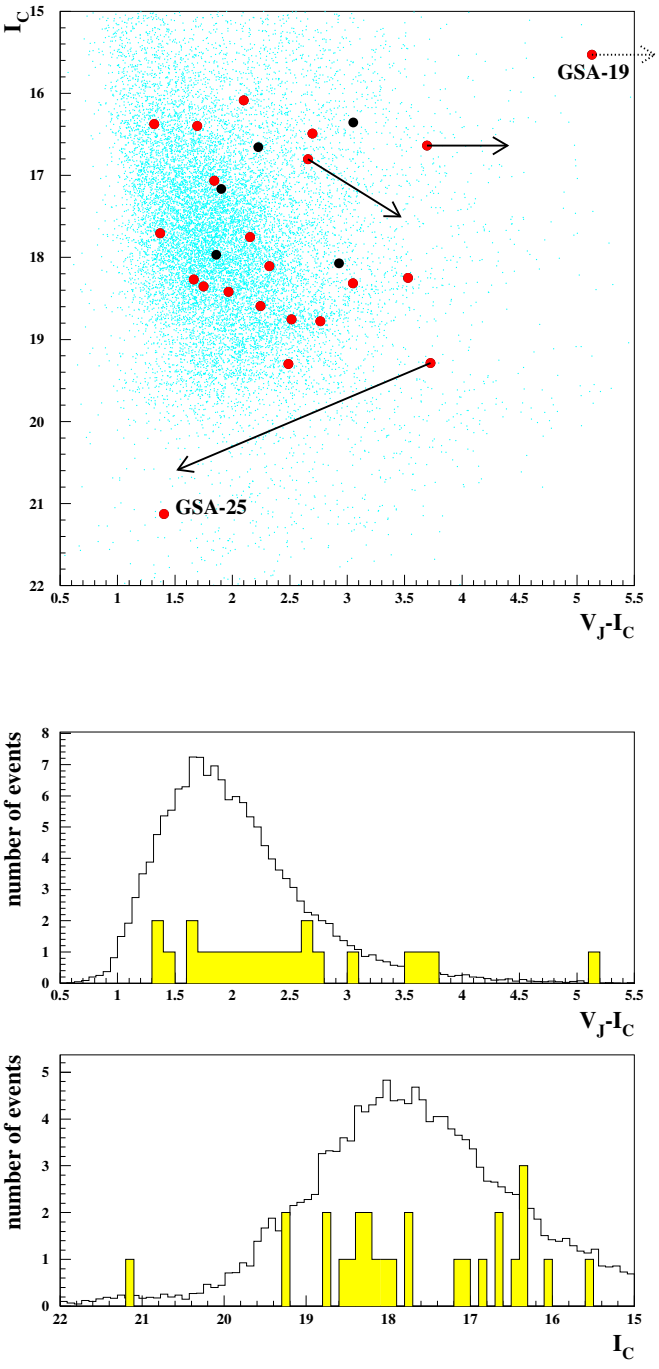

Fig. 10. Color-magnitude diagram and projections of the simulated events satisfying the analysis criteria (small dots) and the detected candidates (big dots). The arrows show $(V_J - I_C, I_C)$ of the magnified component in the case of blending (see notes of table 2). The red dots represent those events that are used for the optical depth estimates. The histograms of these events are superimposed on the projections (not normalized).

lensed sources (obtained by weighting with the optical depth) is significantly biased towards the red color with respect to the simulated distribution of detected sources. We conclude that the distance scattering of the sources can explain the observed bias of the lensed stars towards red color. A more complete interpretation will be provided in a forthcoming publication accordingly to the guidelines given in Sect. 9.

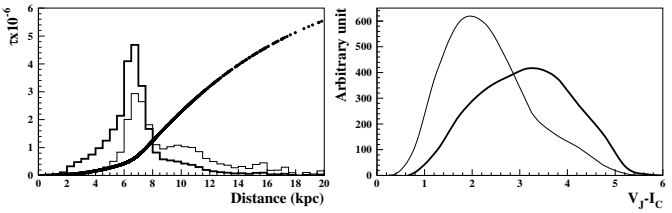

Fig. 11. Left: Optical depth as a function of the distance (thick line), source distance distribution of a simulated catalog (thick histogram), and distance distribution weighted by the optical depth (thin histogram). Right: color distribution of the stars of the simulated catalog (thin line) and expected color distribution of the *lensed* stars (thick line).

Two outliers need a specific comment. On closer inspection, it appears that GSA25 is a genuine microlensing candidate of a very faint star. It was detected because of the very strong magnification. This is a rare case, but there is no reason to discard it from our list. GSA19 is a very bright and very red object. It could be a strongly absorbed nearby star lensed by a closer object.

The spatial distribution of the candidates shown in Fig. 12 does not indicate any remarkable concentration.

6.5. Domain of sensitivity of the analysis

The **C1** and **C2** cuts that use the $\Delta T_{u<2}$ duration of the stage with magnification $A > 1.06$ mainly affect the light-curves which show long bumps. Removing these two cuts adds 6 candidates, all of very long duration, that have a poor signal to noise ratio. As is the case for the GSA-u1 event, only a very long monitoring could change the status of such candidates and improve or degrade their signal to noise ratio. Therefore one should keep in mind that the optical depths we publish in this paper are almost insensitive to events with $t_E > 700$ *days* (cf. the detection efficiency versus t_E curve in Fig. 13).

7. Optical depth

To obtain reliable optical depth values, we use a sub-sample of good quality candidates which should be almost free of the microlensing like variable objects that have been identified towards other EROS targets (Tisserand *et al.* 2007; Hamadache *et al.* 2006) and in Sect. 6.2. For this purpose, we will only keep those candidates that have $u_0 < 0.7$ in the fit that assumes a point-like source and a point-like deflector with a constant speed. This is approximately equivalent to requesting $A_{max} > 1.68$. Events GSA13, 14, 16, 24 and GSAu1 are then discarded for the optical depth analysis.

7.1. Microlensing detection efficiency

We present here the efficiency calculation for the detection of events with $u_0 < 0.7$. As for our previous papers, we calculate our detection efficiency by superimposing simulated events on measured light curves from an unbiased sub-sample of our catalog. Events are simulated as point-source, point-lens constant velocity microlensing events, with parameters uniformly spanning a domain largely exceeding the domain of EROS sensitivity (u_0 up to 2, 1 *day* $< t_E <$ 900 *days*, t_0 generated from 150 days before the first observation to 150 days after the last). Efficiency is defined as the ratio of events satisfying the selection cuts to the

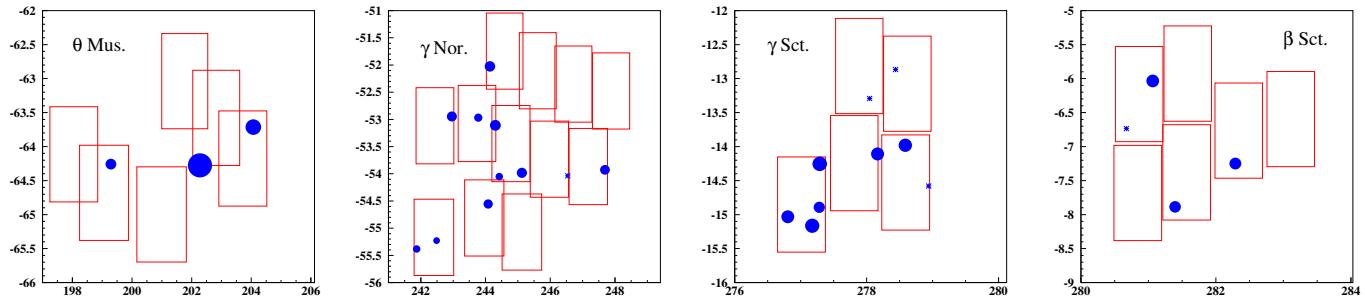

Fig. 12. From left to right: spatial distribution (α, δ) of the 27 candidates in the monitored fields towards θ Mus, γ Nor, γ Sct and β Sct. East is right, North is up. The area of a marker is proportional to the contribution of the candidate to the optical depth towards the corresponding target. Events with $u_0 > 0.7$ are marked with a star.

number of events generated up to $u_0 = 1$. Figure 13 (upper left panel) shows the EROS efficiency as a function of the source position in the color-magnitude diagram averaged over all the other parameters and over all directions. The other frames of Fig. 13 show the efficiency as a 2D-function of I_C of the lensed star and t_E, and as a 1D-function of t_E, u_0, I_C and $V_J - I_C$, averaged over all the other parameters, for each monitored direction. The efficiency is significantly better towards γ Nor, because of the higher sampling of the light curves in this direction.

7.2. Optical depth determination

The optical depth values obtained from the 22 events that satisfy $u_0 < 0.7$ are given in the first part of table 3. The average over all directions is defined as the proportion of stars covered by an Einstein disk. It is given by

$$\bar{\tau}_{fields} = \frac{\sum_i N^i_* \tau_i}{\sum N^i_*} \text{ with } \tau_i = \frac{\pi}{2} \frac{1}{N^i_* \Delta T^i_{obs}} \sum_{events} \frac{t_E}{\epsilon^i(t_E)},$$

where N^i_*, ΔT^i_{obs}, $\epsilon^i(t_E)$ are respectively the number of stars monitored, the observation duration and the microlensing selection efficiency towards direction i. As usual, selection efficiency is relative to events with $u_0 < 1$ (even though the efficiency is almost zero for $u_0 > 0.7$). As explained at the end of Sect. 5.4, we use $\frac{t_E(best\ fit)}{\epsilon(t_E(standard\ fit))}$ in the expression of τ for non-standard microlensing events. The statistical uncertainties are estimated from the definition of the classical 68% confidence intervals (Feldman & Cousins 1998), multiplied by the factor

$$\frac{\sqrt{< t_E^2/\epsilon^2(t_E) >}}{< t_E/\epsilon(t_E) >}, \quad (16)$$

following Han & Gould 1995. According to the discussion of Sect. 4.1, we assume a 10% maximum systematic uncertainty due to blending effects, as in Afonso *et al.* 2003, and we account for another 5% uncertainty due to the statistical limitations in the determination of the efficiencies. These errors are small compared to the smallest statistical uncertainty ($\sim$ 30%) estimated in this paper.

7.3. Robustness of the optical depth values

We have studied the stability of the optical depth averaged over all fields by changing the selection cuts. Fig. 14 gives the variation of $\bar{\tau}_{fields}$ with the $\Delta\chi^2$ threshold. Relaxing this threshold makes the optical depth increase rapidly, due to the inclusion of false events, as a logical result of the analysis optimization.

	θ Mus	γ Nor	γ Sct	β Sct	
b°	-1.46	-2.42	-2.09	-2.15	
l°	306.56	331.09	18.51	26.60	
Observations					All
$\tau \times 10^6$	$.67^{+.63}_{-.52}$	$.49^{+.21}_{-.18}$	$.72^{+.41}_{-.28}$	$.30^{+.23}_{-.20}$	$.51^{+.13}_{-.13}$
N_{events}	3	10	6	3	22
$\bar{t_E}$ (days)	97 ± 47	57 ± 10	47 ± 6	59 ± 6	60 ± 9
σ_{t_E}	80	29	13	10	40
ϵ corrected $\bar{t_E}$	65 ± 45	43 ± 10	45 ± 6	58 ± 6	48 ± 9
ϵ corrected σ_{t_E}	75	31	13	9	38
median t_E	74.2	64.	47.2	55.	56.5

	τ ($\times 10^6$) **from models**				χ^2_{model}
A	0.32	0.48	0.79	0.60	2.3
+spiral	0.56	0.69	1.07	0.83	7.9
B	0.34	0.51	0.85	0.64	2.9
+spiral	0.61	0.72	1.13	0.90	10.2
C	0.47	0.78	1.11	0.95	12.5
+spiral	0.71	1.18	1.43	1.23	36.1
D	0.32	0.56	0.41	0.38	1.4
model 1	0.42	0.52	0.71	0.57	1.8
model 2	0.54	0.68	0.90	0.74	5.4

	Predictions from model 1			
N_{events}	2.8	9.9	7.1	6.3
$\bar{t_E}$	73.8	67.9	37.9	60.2
σ_{t_E}	63	54	36	48
median t_E	54.5	52.5	28.0	46.5
	$\bar{t_E}$ **from published models**			
C (no effic.)	45	28	25	27
C+spiral	38	38	44	40
D	80.9	86.5	76.9	77.4

Table 3.
- Observed optical depth τ, number of events N_{events}, average $\bar{t_E}$, dispersion σ_{t_E}, efficiency corrected $\bar{t_E}$ and σ_{t_E} and median time scale for each monitored direction. Here, we consider only the events used for the optical depth estimates (*i.e.* with $u_0 < 0.7$).
- Optical depth predictions from models A, B, C, including or not a spiral structure (see text), and from model D, and estimates up to 7 kpc from the two simple Galactic models described in table 4. The χ^2's quantify the adequation with the observations (see Sect. 8).
- Expected numbers of events and duration distribution parameters from model 1 and from models C and D. $\bar{t_E}$ from model C do not take into account the detection efficiency.

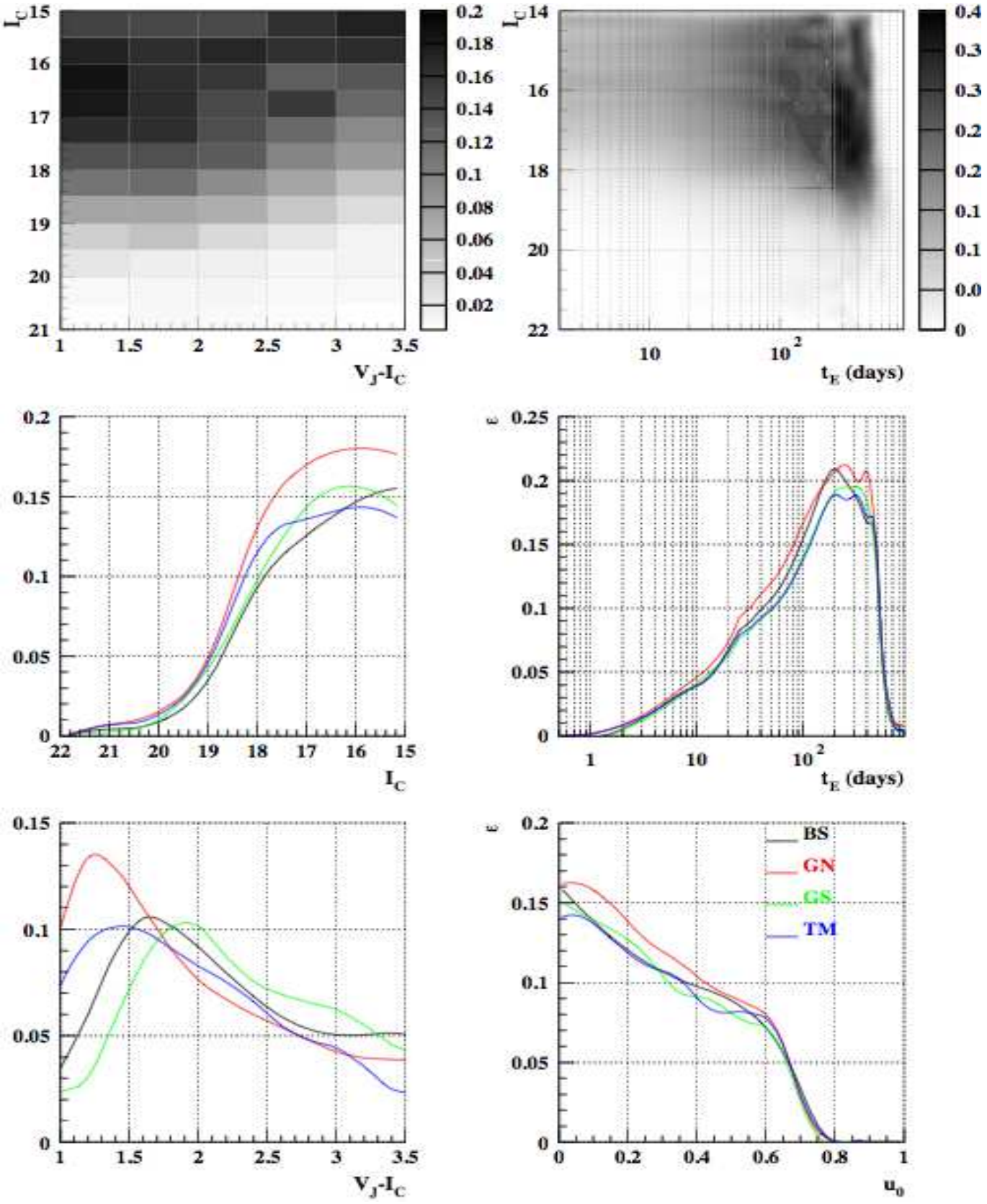

Fig. 13. Microlensing detection efficiency.
Upper left: the efficiency in the $(V_J - I_C, I_C)$ plane averaged over u_0, t_0, t_E and over the 4 monitored fields.
Upper right: the efficiency in the (t_E, I_C) plane averaged over u_0, t_0, $V_J - I_C$ and over the 4 monitored fields.
Other panels: efficiency as a function of the lensed star magnitude I_C, as a function of the color index $(V_J - I_C)$ and as a function of the event parameters t_E and u_0. Each curve gives the efficiency averaged over all the other parameters.

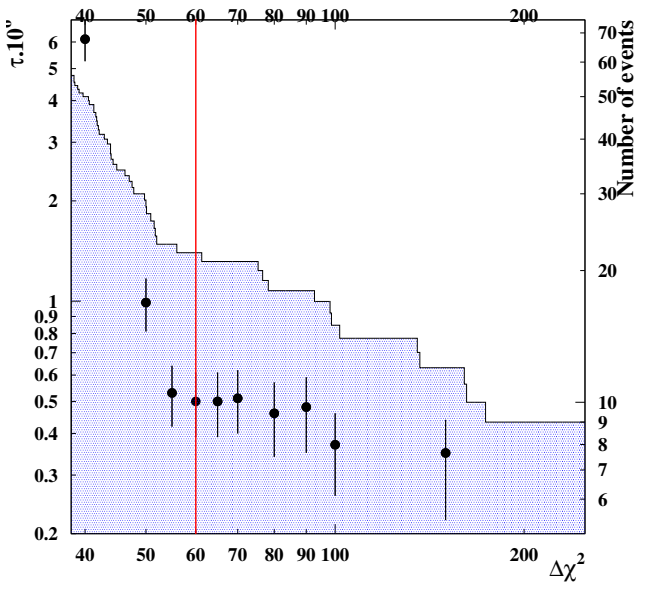

Fig. 14. Variation of the number of selected candidates (histogram, right scale) and of $\bar{\tau}_{fields}$ (dots, left scale) with the $\Delta\chi^2$ threshold. The red vertical line shows our cut. Only statistical errors are plotted.

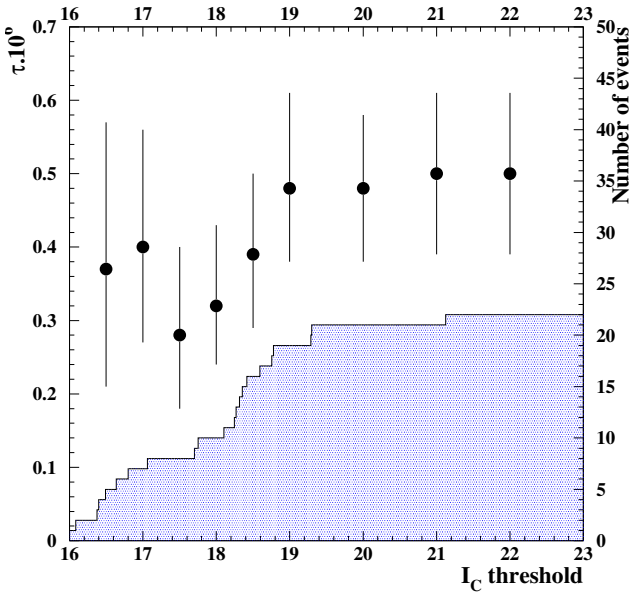

Fig. 16. Number of selected candidates (histogram, right scale) and $\bar{\tau}_{fields}$ (dots, left scale) for the sub-samples of stars brighter than the I_C threshold. Only statistical errors are plotted.

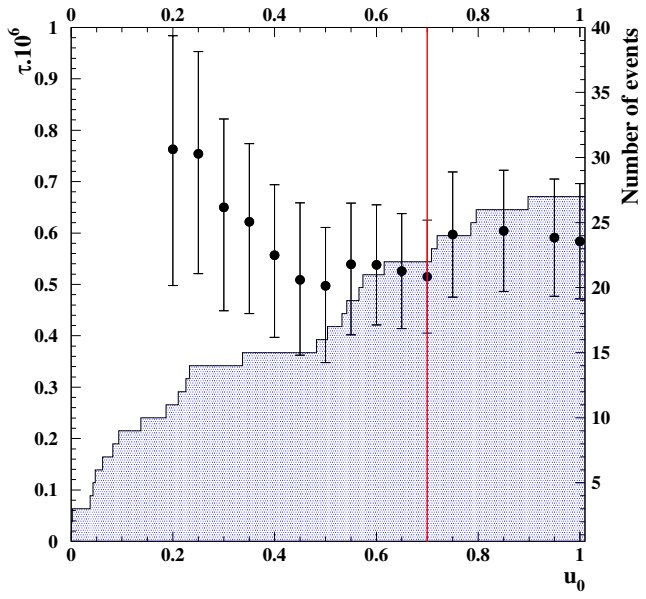

Fig. 15. Variation of the number of selected candidates (histogram, right scale) and of $\bar{\tau}_{fields}$ (dots, left scale) with the u_0 threshold. The red vertical line corresponds to our selection. Only statistical errors are plotted.

But using a stricter cut does not significantly change the optical depth values, as long as the statistics remains significant.

Fig. 15 also gives $\bar{\tau}_{fields}$ as a function of the u_0 threshold. Our result does not depend on this cut within statistical errors, showing that we probably found an optimum between the quality of the events and the number of those kept for our optical depth calculations.

Fig. 16 and 17 show the variation of $\bar{\tau}_{fields}$ with the maximum magnitude I_c of the source population and with the minimum color index $V_J - I_C$. There is no evidence for a variation with I_C threshold. As discussed below in Sect. 9.3, this comes from the fact that the variation of the optical depth with the distance does not result in a variation with the magnitude as more distant identified sources do not appear fainter in our catalog on average. Interestingly one may use these figures to extract τ for specific stellar populations, in particular the population of the brightest stars with $I_C < 18.5$ that are better identified and measured, and that suffer less blending (see Sect. 4.1). Moreover, our catalog is almost complete up to this magnitude, as our star detection efficiency is large (see Fig. 4). Using such a sub-catalog of bright stars should make the interpretation easier within a Galactic model framework as will be discussed hereafter.

8. Discussion: comparisons with simple models

8.1. Optical depth

We will consider here 4 published optical depth calculations and our own calculations based on simple Galactic models (model 1 without a thick disk, model 2 with a thick disk) that we already used for discussions in papers I and II. The main revision to these 2 models since our previous papers comes from the bulge inclination; we now take $\Phi = 45°$ instead of 15° (Hamadache *et al.* 2006 and Picaud & Robin 2004) as the angle of the outer bulge with respect to the line of sight towards the Galactic center. The only impact of this change is a little variation of our optical depth value towards γ Sct. We also completely neglect any contribution from the halo to the optical depth, in the light of the latest EROS results towards the Magellanic Clouds (Tisserand *et al.* 2007). As in our previous papers, we performed simple optical depth calculations assuming all the sources to be at the same distance. More sophisticated modelling based on the

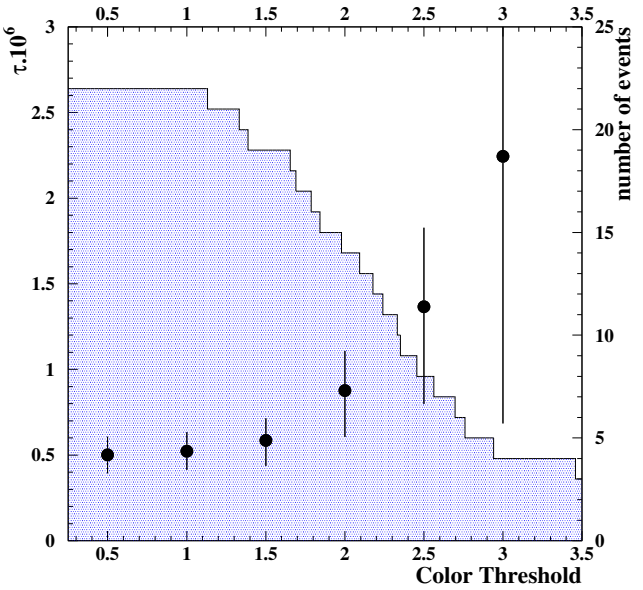

Fig. 17. Number of selected candidates (histogram, right scale) and $\bar{\tau}_{fields}$ (dots, left scale) for the sub-samples of stars redder than the color index $(V_J - I_C)$ threshold. Only statistical errors are plotted.

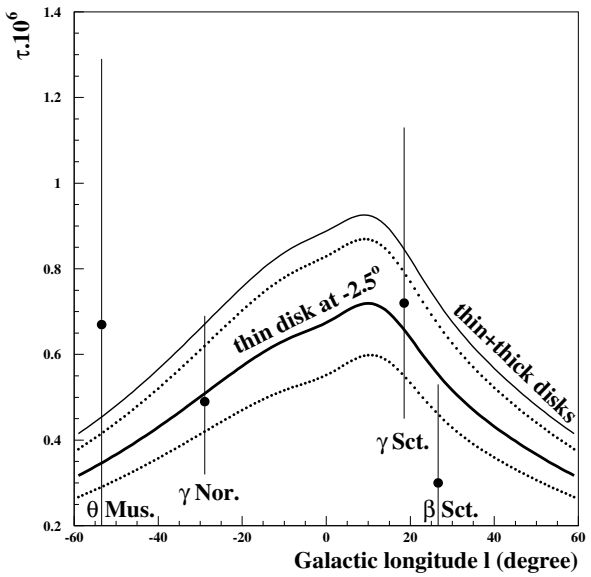

Fig. 18. Expected optical depth up to 7 *kpc* at a Galactic latitude $b = -2.5°$ for model 1 (thick curve) and model 2 (thin curve) which assumes an additional thick disk. The dotted lines show the excursion of the model 1 predictions when varying the latitude by ±1°. The measured optical depths are given for our 4 targets.

Table 4. Parameters of the Galactic models 1 and 2 used in this article.

	Parameter	model 1	model 2
	$R_\odot$ (kpc)	8.5	
Thin disk	Σ ($M_\odot$pc^{-2})	50	
	H (kpc)	0.325	
	R (kpc)	3.5	
	$M_{thin}(\times 10^{10} M_\odot)$	4.3	
	σ_r ($km\ s^{-1}$)	34.	
	σ_θ ($km\ s^{-1}$)	28.	
	σ_z ($km\ s^{-1}$)	20.	
Thick disk	Σ ($M_\odot$pc^{-2})	-	35
	H (kpc)	-	1.0
	R (kpc)	-	3.5
	$M_{thick}(\times 10^{10} M_\odot)$	-	3.1
	σ_r ($km\ s^{-1}$)	-	51.
	σ_θ ($km\ s^{-1}$)	-	38.
	σ_z ($km\ s^{-1}$)	-	35.
Bulge	a (kpc)	1.49	
	b (kpc)	0.58	
	c (kpc)	0.40	
	Inclination Φ	45°	
	$M_B(\times 10^{10} M_\odot)$	1.7	
	σ_{bulge} ($km\ s^{-1}$)	110.	

guidelines discussed in Section 9 will be considered in a forthcoming paper. We give in table 4 the list of the geometrical and kinematical parameters used in these models I and II. The disk densities are modeled by a double exponential expressed in cylindrical coordinates:

$$\rho_D(R,z) = \frac{\Sigma}{2H} \exp\left(\frac{-(R-R_\odot)}{h}\right) \exp\left(\frac{-|z|}{H}\right) ,$$

where Σ is the column density of the disk at the Sun position $R_\odot$, H the height scale and h the length scale of the disc. The density distribution for the bulge - a bar-like triaxial model - is taken from Dwek *et al.* 1995 model G2, given in Cartesian coordinates:

$$\rho_B = \frac{M_B}{6.57\pi abc} e^{-r^2/2} , \; r^4 = \left[\left(\frac{x}{a}\right)^2 + \left(\frac{y}{b}\right)^2\right]^2 + \frac{z^4}{c^4} ,$$

where M_B is the bulge mass, and a, b, c the length scale factors. Fig. 18 shows the measured optical depth as a function of the Galactic longitude, with the expectations from models 1 and 2 at 7 *kpc* and at a Galactic latitude $b = -2.5°$. We also show in this figure the effect of a Galactic latitude change by ±1°.

The optical depth predictions of model 1 and 2 and of the 4 following models are reported in table 3:

- **Model A**, from Binney *et al.* 1997, revised by Bissantz *et al.* 1997, has a cuspy and flat Galatic bar, inclined by $\Phi \sim 20°$.
- **Model B**, described in Dwek *et al.* 1995, has a wider cuspy bar, inclined by $\Phi \sim 24°$.
- **Model C**, described in Freudenreich 1998, has a more extended and diffuse bar, inclined by $\Phi \sim 14°$.

The optical depths towards the directions monitored by EROS have been calculated for these 3 models and discussed by Evans & Belokurov 2002, who have also included the contribution from the disk and considered separately the impact of a spiral structure. These 3 models have been normalized to have the same total mass ($1.5 \times 10^{10} M_\odot$) within 2.5 kpc. Therefore, they mainly differ by the shape details and the orientation of the bar.

- **Model D**, described in Grenacher *et al.* 1999, has a bar that is similar to the one of our models 1 or 2, but inclined by $\Phi \sim 20°$, with a combination of a light thin disk plus a thick disk and a halo contribution.

The adequation of all these models with the observed optical depths τ can be compared through the value of

$$\chi^2_{model} = \sum_{targets\ i} \frac{(\tau_i(model) - \tau_i(observed))^2}{\sigma_i^2}, \quad (17)$$

where σ_i is the error interval of the τ_i determination (as errors are asymmetrical, we consider the largest one for each measurement). The numbers reported in table 3 show that our model 1 is clearly favored by the data, and also models A and D without spiral structure, which are the ones that predict the smallest optical depths.

We cannot draw more conclusions about our model 1, as we know that it is not a realistic description, since all targets are supposed to be at the same distance. One may also notice that the extrapolation of any *bulge* model to the relatively distant region that we monitored is very uncertain. Nevertheless, it seems that "heavy" models trying to include a thick disk or any spiral structure are not favored. These results confirm the conclusions of Hamadache *et al.* 2006, in particular for model C, that is also disfavored by the present data.

8.2. Event duration distribution

Fig. 19 gives the t_E distributions for the observed events, compared to the expected distributions from model 1. The procedure to build these distributions is the same as in paper II:

- The mass function for the lenses is taken from Gould, Bahcall & Flynn 1997 for both the disk and the bulge.
- The solar motion with respect to the disk is taken from (Delhaye 1965):

$$v_{\odot R} = -10.4,\ v_{\odot\theta} = 14.8,\ v_{\odot z} = 7.3\ \ (\mathrm{km/s}). \quad (18)$$

- The global rotation of the disk is given by

$$V_{rot}(r) = V_{rot,\odot} \times \left[1.00762 \left(\frac{r}{R_\odot}\right)^{0.0394} + 0.00712\right], \quad (19)$$

  where $V_{rot,\odot} = 220$ km/s (Brand & Blitz 1993).
- The peculiar velocity of disk stars is described by an anisotropic Gaussian distribution and a velocity dispersion given in table 4.
- The velocity distribution of the bulge stars is given by

$$f_T(v_T) = \frac{1}{\sigma^2_{bulge}} v_T \exp\left(-\frac{v_T^2}{2\sigma^2_{bulge}}\right), \quad (20)$$

  with $\sigma_{bulge} \sim 110$ km/s.

The Kolmogorov-Smirnov tests indicate that model 1 produces t_E distributions that are fully compatible with the observations, except for γ Sct where the approximation of a single distance for all the sources is the most questionable (due to the contribution of the sources belonging to the elongated bulge). Nevertheless, the supplement of short events towards this direction that is visible in the t_E distribution corresponds to the expectations from bulge lenses. We found that our simulation results are not dramatically changed if we change the contribution of the lightest lens objects (around $0.1 M_\odot$) by 50%. This is mainly due to the low detection efficiency for the short events expected from low mass lenses (this loss of efficiency is specially noticiable for low mass bar lenses because their velocity is larger).

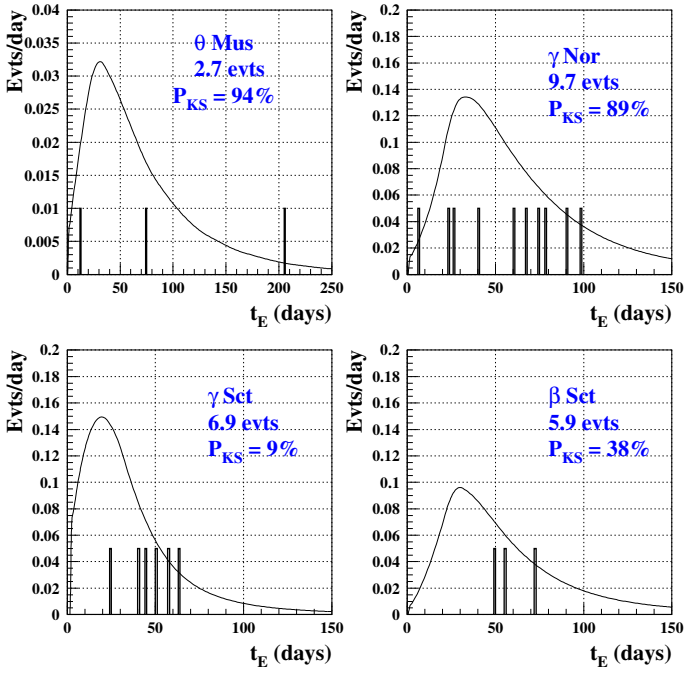

Fig. 19. measured t_E distributions compared to the one calculated with our model 1 for one day intervals. P_{KS} gives the Kolmogorov-Smirnov test probability of compatibility of the shapes. Notice that the scales are different for θ Mus. The t_E values of the observed events are given by the vertical bars.

Table 3 gives the observed averages, dispersions and medians of t_E, with the predictions from model 1 and models C and D. Only mean duration predictions have been estimated for model C (with no efficiency corrections) and D (taking into account EROS microlensing detection efficiency). The general tendency that emerges from the observations and that is confirmed by the predictions is that $\bar{t_E}$ increases with the Galactic longitude. This is due to the fact that the direction of global motion of the lenses tends to align with the line of sight when the longitude increases, and consequently the transverse speed becomes smaller.

As the variation of the microlensing detection efficiency with t_E is not taken into account in the predictions of model C, we should compare here the $\bar{t_E}$ predicted values with the efficiency corrected means given by

$$\frac{\sum_{events} t_E/\epsilon(t_E)}{\sum_{events} 1/\epsilon(t_E)}. \quad (21)$$

The observed corrected means are significantly larger than the predictions of model C with no spiral structure. This discrepancy could be explained (at least partially) by the absence of very short time scale events that have a negligible detection efficiency and can be totally missed in our statistically limited sample; a more precise comparison could be done between the observed t_E distribution and a modified predicted distribution taking into account the microlensing detection efficiency as a function of t_E (Fig. 13). Keeping in mind the possibility of undetectable events, it seems that model C without spiral structure is disfavoured. Evans & Belokurov 2002 have emphasized the impact of streaming in the bar on the t_E distribution around the Galactic center and the impact of the spiral structure on $\bar{t_E}$ in ev-

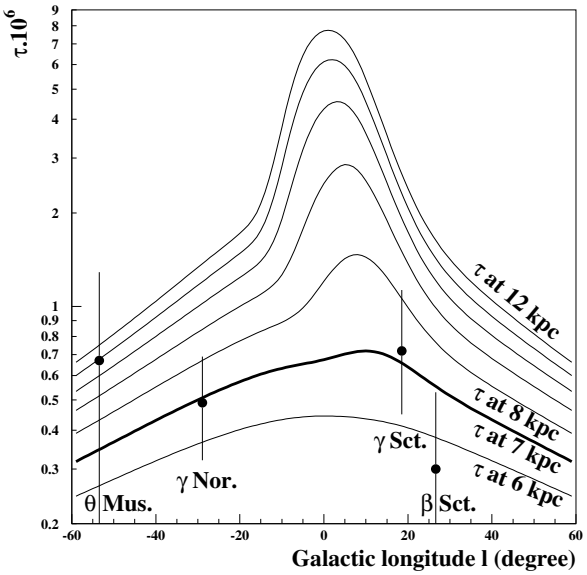

Fig. 20. Model 1 predictions for the optical depth at 6, 7, 8, 9, 10, 11 and 12 kpc (from lowest to highest curve) at a Galactic latitude $b = -2.5°$ as a function of the Galactic longitude. The measured optical depths are given for our 4 targets.

ery direction. Such a streaming and the spiral structure have a serious impact on the $\bar{t_{\rm E}}$ values, and could reconcile the model expectations with the t_E data, but lighter disk and spiral structure should be considered to fit the optical depth data as well. There is probably some margin of freedom for doing this, as model C is obtained from the extrapolation of the light distribution at latitudes larger than 5°.

The mean durations predicted by Grenacher *et al.* 1999 (model D) take into account the EROS efficiencies. Therefore, we can directly compare the predictions with our (uncorrected) $\bar{t_{\rm E}}$ values. This model predicts longer durations than observed, but here again it seems that the predictions could be adjusted, as they are sensitive to the value of the minimal lens mass.

9. Guidelines for further interpretation

As we always emphasized when presenting previous results towards the spiral arms, the fact that the distance distribution of the target sources is poorly known complicates the optical depth interpretation. Fig. 20 shows the expected optical depth as a function of the Galactic longitude l, for different target distances, using model 1. This figure shows first that the impact of the bulge on the optical depth is significant only towards γ Sct. One also sees that the optical depth to distances smaller than 12 kpc is larger for $l > 0$, the near side of the bulge, because the number density of *lenses* is larger on this side; but on the contrary, the OGLE II collaboration (Udalski *et al.* 2000a) reported a larger rate for $l < 0$ than for $l > 0$ in their catalog of microlensing events in the Galactic bulge. This is due to the fact that the optical depth *averaged* over all distances can be larger for $l < 0$, the far side of the bulge, because there are more distant *sources* on this side, with a larger optical depth. The observed asymmetry should then depend on the selection of the monitored sources. This illustrates the difference between the optical depth up to a given distance, and the average optical depth over a set of stars located at various distances. Therefore, we provide here guidelines to interpret our optical depth values within a Galactic model framework.

9.1. The concept of "catalog optical depth"

The EROS measured optical depth is the average over the distance distribution of the monitored sources. Establishing this distance distribution through individual spectrophotometric measurements would require an enormous amount of complementary observations. This leads us to define the concept of "catalog optical depth" τ_{cat}, which is relative to a particular catalog of monitored stars: τ_{cat} is defined as the fraction of stars *of a given catalog* that undergo a magnification $A > 1.34$. Our *measured* optical depth can be compared with the depth derived from a lens and source distribution model as follows: first, one has to generate a synthetic source catalog that matches our own catalog, taking into account the EROS star detection efficiency (Fig. 4); then one can use the generated source distance distribution to estimate the average optical depth and compare it with the measurements. This procedure is described in more detail below.

9.2. Synthesizing a catalog that matches the EROS one

Let $S_{model}(D, M_I, M_V - M_I)$ be the source number density predicted by the model as a function of the distance D and of the *absolute* magnitude M_I and color $M_V - M_I$; let $A_I(D)$ and $A_V(D)$ be the predicted absorptions in I and V. The pre-requisite for an optical depth interpretation is that $n_{cat}(I, V - I)$, the density per solid angle per *apparent* magnitude and color index of the synthesized source catalog, fits the observed one within the visible color-magnitude diagram. This density is related to $S_{model}(D, M_I, M_V - M_I)$ as follows:

$$n_{cat}(I, V-I) = \int_0^\infty S_{model}(D, M_I, M_V - M_I)\epsilon_{star}(B_{EROS})D^2 {\rm d}D \quad (22)$$

where $\epsilon_{star}(B_{EROS})$ is our star detection efficiency given in Fig. 4 as a function of $B_{EROS} = I + 0.6(V - I)$ *apparent* B magnitude in the EROS system. For given I and $V - I$ apparent magnitude and color, M_I and $M_V - M_I$ depend on the distance D as follows:

$$\begin{aligned} M_I &= I - 2.5\log(D/10kpc) - A_I(D), \quad (23)\\ M_V - M_I &= V - I - A_V(D) + A_I(D). \end{aligned}$$

For the comparison with the observations, the color-magnitude diagrams $n_{eros}(I, V - I)$ of our catalogs (Fig. 5) should be used. They provide the observed stellar density per unit solid angle in the effectively monitored field, that is corrected for the dead regions of our CCDs, the overlap between fields and the blind regions around the brightest objects.

We show here the color-magnitude diagram of a preliminary catalog obtained with this procedure (Fig. 21). This catalog has been produced for the qualitative understanding of the observed diagrams (Sect. 4.2, Fig. 5) and also of the color bias of the lensed population (Sect. 6.4.2, Fig. 11). For this simulation, we considered a stellar population identical to the one of the solar neighborhood (ESA 1997, Turon *et al.* 1995), distributed according to the disk and bulge mass distributions described in Sect. 8; the reddening was calculated assuming the following absorption law (Weingartner & Draine, 2001):

$$A(V)/N_H = 5.3 \times 10^{-22} cm^2 \quad A(I)/N_H = 2.6 \times 10^{-22} cm^2, \quad (24)$$

where N_H is the column-density of neutral hydrogen (atomic plus molecular), assumed to represent 4% of the mass density.

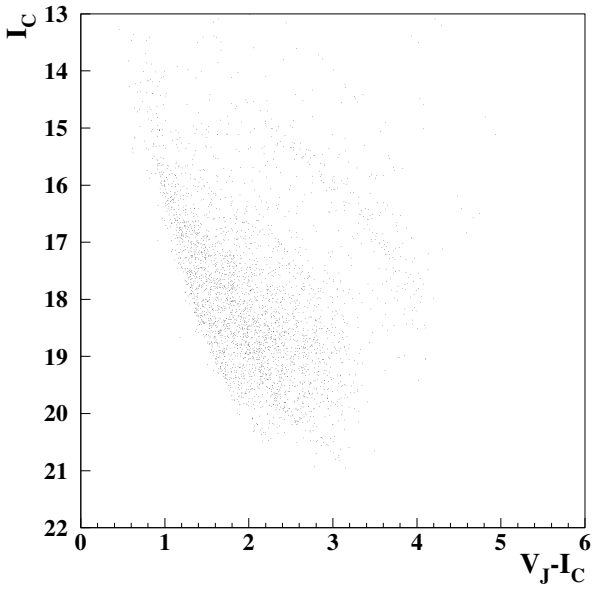

Fig. 21. Simulated color-magnitude diagram towards γ Sct (see text).

The catalog was simulated using our star detection efficiency of Fig. 4. Fig. 11(left) shows the source distance distribution of the catalog thus obtained. This catalog will be finalized in a forthcoming paper.

9.3. Estimating the average optical depth

Once the synthesis of a catalog is performed, one can compute the average optical depth over the synthesized catalog:

$$< \tau_{model} >= \frac{\int_0^\infty n_{model}(D)\tau_{model}(D)D^2\,\mathrm{d}D}{\int_0^\infty n_{model}(D)D^2\,\mathrm{d}D}, \quad (25)$$

where $\tau_{model}(D)$ is the predicted optical depth at distance D and

$$n_{model}(D) = \quad (26)$$
$$\iint S_{model}(D, M_I, M_V - M_I) \cdot \epsilon_{star}(B_{EROS})\,\mathrm{d}M_I\,\mathrm{d}(M_V - M_I)$$

is the number density of stars (per solid angle and distance unit) located at distance D that enters the catalog. $B_{EROS} = I + 0.6(V - I)$ is obtained from M_I, $M_V - M_I$ and D through equations (23).

This procedure assumes that the average microlensing detection efficiency does not vary significantly with the distance of the sources. This is indeed the case because both the efficiency of our star detector and the average microlensing detection efficiency depend on the *apparent* magnitudes. The microlensing detection efficiency averaged on distant *detected* stellar populations is then similar to the one averaged on nearby detected populations because their apparent magnitude distributions are both peaked around the limiting magnitude. We have checked these features with simulations using our star detection efficiencies.

The observed optical depths in Table 3 are relative to our entire catalogs. We recall here the average value for the 4 targets (12.9×10^6 stars):

$$\bar{\tau}_{full\ catalog} = 0.51 \pm 0.13 \times 10^{-6}.$$

For easier comparisons, we extract from Fig. 16 the following optical depth

$$\bar{\tau}(I_c < 18.5) = 0.39 \pm .11 \times 10^{-6},$$

relative to the sub-set of 6.52 million stars brighter than $I_c = 18.5$, for which our catalog is close to being complete.

10. Conclusions

The microlensing event search of EROS2 towards transparent windows of the spiral arms leads to optical depths that are consistent with a very simple Galactic model. The possibility of a long bar that was proposed in our paper II as a possible explanation of the observed optical depth and duration asymetries is not confirmed; indeed, the inclination of the bar was revised since the time of this publication, and the final optical depth measured towards γ Sct is also smaller (but statistically compatible). A more complete interpretation that would take into account the distance distribution of the monitored sources needs a model that allows one to synthesize the EROS catalogs of these sources. With such a model, one would also be able to make use of the event duration distributions.

The VISTA project with its wide field infrared camera appears to offer an excellent opportunity to improve our knowledge of the microlensing towards the Galactic plane. The infrared light will allow the observers to monitor stars through dust, making them free of the transparent windows that were limiting the EROS fields.

Acknowledgements. We are grateful to the technical staff at ESO, La Silla for the support given to the EROS-2 project. We thank J-F. Lecointe and A. Gomes for the assistance with the online computing and the staff of the CC-IN2P3, especially the team in charge of the HPSS storage system, for their help with the data management.

11. Annex A

References

Afonso C., Albert J.-N., Andersen J. *et al.* (EROS Coll.), 2003, A&A, 400, 951
Alcock C., Akerlof C.W., Allsman R.A. *et al.* (MACHO Coll.), 1993, Nat, 365, 621
Alcock C., Allsman R.A., Alves D. *et al.*, 2000, ApJ, 542, 281
Ansari R., 1996, Vistas in Astronomy, 40, No 4
Aubourg É., Bareyre P., Bréhin S. *et al.* (EROS Coll.), 1993, Nat, 365, 623
Bennett D. P., 2005, ApJ, 633, 906
Binney J., Gerhard 0., & Spergel D., 1997, MNRAS, 288, 365
Bissantz N., Englmaier P., Binney J., & Gerhard 0.E., 1997, MNRAS, 289, 651
Bissantz, N. and Gerhard, O. 2002, MNRAS, 330, 591
Brand J., Blitz L., 1993, A&A, 275, 67
Calchi Novati S., De Luca F., Jetzer Ph. *et al.*, 2008, A&A, 480, 723
Derue F., Afonso C., Alard C. *et al.* (EROS Coll.), 1999, A&A, 351, 87
Derue F., Afonso C., Alard C. *et al.* (EROS Coll.), 2001, A&A, 373, 126
Derue F., 1999b, Ph.D. thesis, CNRS/IN2P3, LAL report 99-14, Université Paris 11.
Delhaye J. 1965, in Galactic Structure, The University of Chicago Press
Dwek E., Arendt R.G., Hauser M.G. *et al.*, 1995, ApJ, 445, 716
Epchtein N., Deul E., Derriere S. *et al.*, 1999, A&A, 349, 236
Evans N.W. & Belokurov V., 2002, ApJ, 567, L119
Feldman G.J. & Cousins R.D., 1998, Phys.Rev. D, 57, 3873
Freudenreich H.T., 1998, ApJ, 492, 495
Gould, A. 1992, ApJ , 392, 442
Gould A., Bahcall J.N., Flynn C., 1997, ApJ, 482, 913
Grenacher L. *et al.*, 1999, A&A, 351, 775
Hamadache C., Le Guillou L., Tisserand P. et al., 2006, A&A, 454, 185
Han C., Gould A., 1995, ApJ, 449, 521
Hardy S.J. & Walker M.A., 1995, MNRAS, 276, L79
The Hipparcos and Tycho Catalogs, ed. M.A.C. Perryman (SP-1200; Noordwijk: ESA)
HST archive, https://archive.stsci.edu/

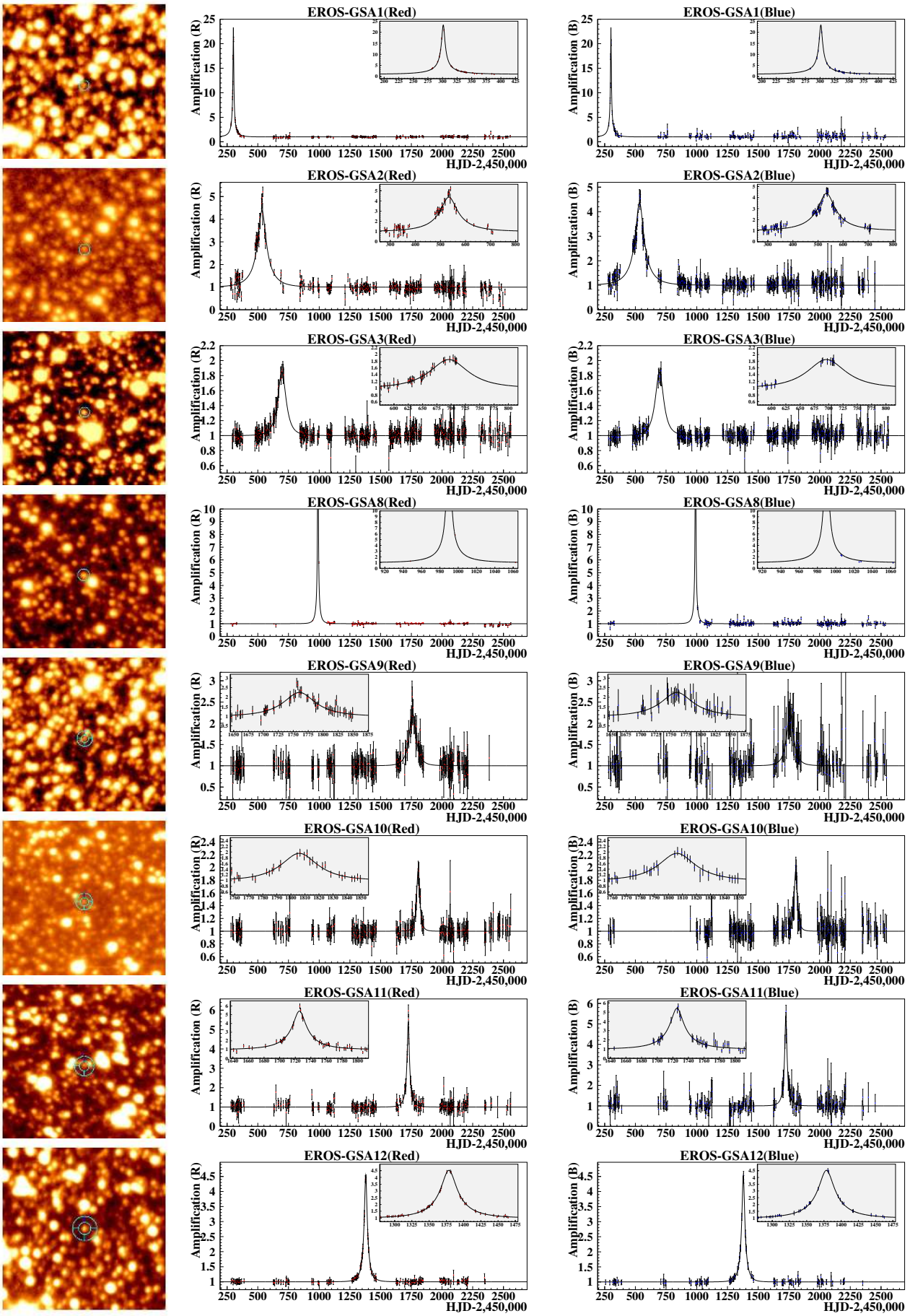

Fig. 22. Finding charts (84″×84″, N-up, E-left) and magnification of the candidates as a function of the Heliocentric Julian Day ($HJD-2,450,000$). In the case of multi-detected events, we display only the best sampled light curve.

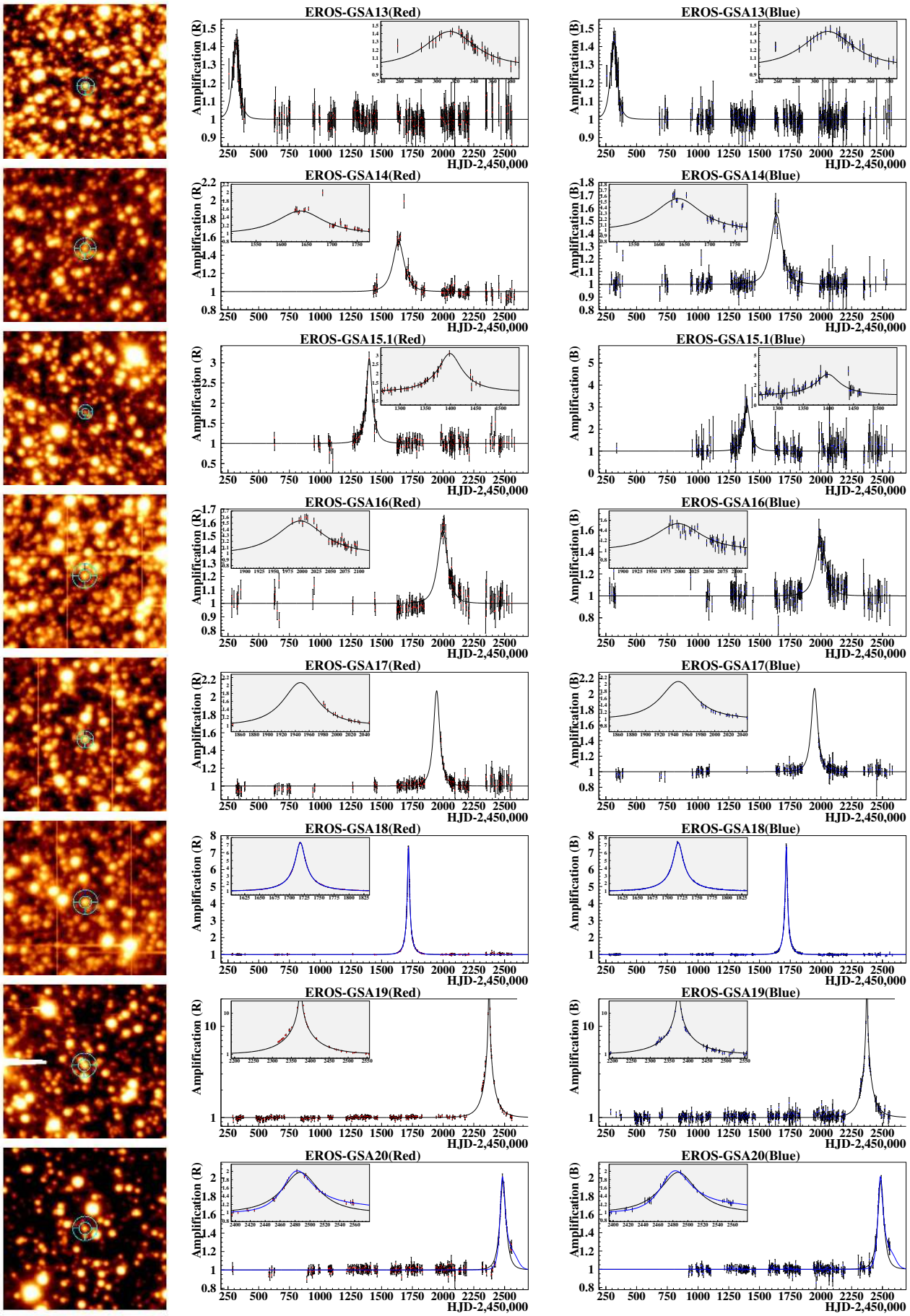

Fig. 23. Light curves and finding charts (continued)

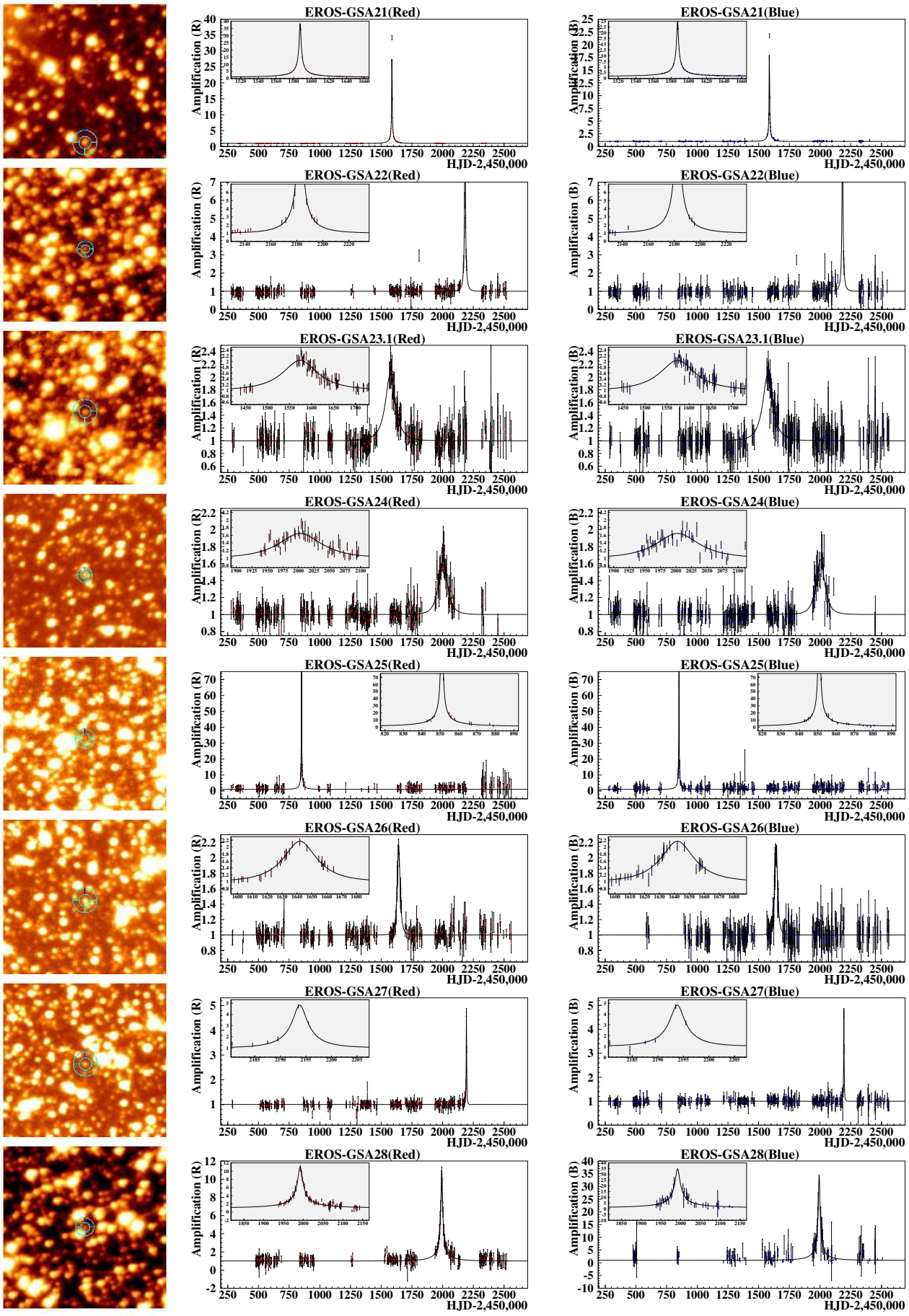

Fig. 24. Light curves and finding charts (continued)

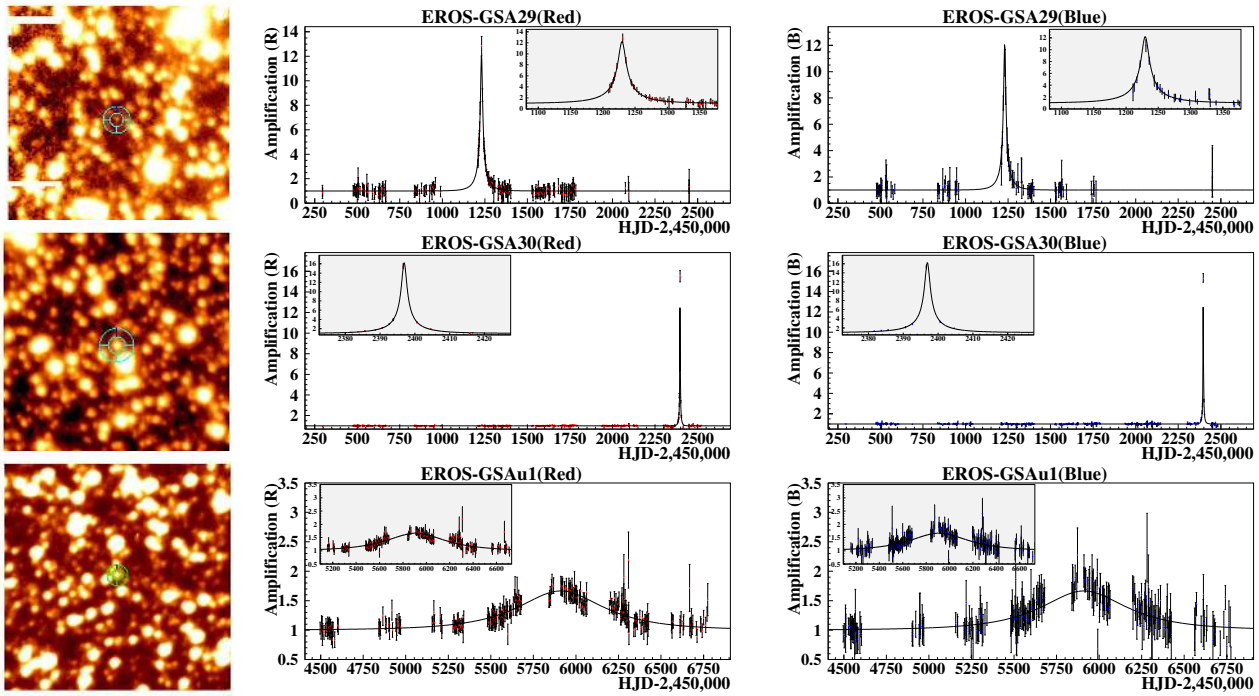

Fig. 25. Light curves and finding charts (continued)

Mao S., Stefano R.D., 1995, ApJ, 440, 22
Möllerach S., Roulet E., 2002, Gravitational lensing and microlensing, World Scientific
OGLE web page http://www.astrouw.edu.pl/ ogle/ogle2/fields.html
Paczyński B., 1986, ApJ, 304, 1
Picaud S., Robin A.C., 2004, A&A, 428, 891
Popowski, P., Griest, K., Thomas, C. L., *et al.*, 2005, ApJ, 631, 879
Rahal Y. R., 2003, Ph.D. thesis, Université Paris 6 LAL-CNRS/IN2P3 report 03-85
Rahvar, S., 2004, MNRAS, 347, 213
Sumi, T., Wozniak, P. R., Udalski, A., *et al.* (OGLE coll.), 2006, ApJ, 636, 240
Tisserand P., 2004, Ph.D. thesis, Université de Nice-Sophya Antipolis CEA DAPNIA-04-09-T
Tisserand P. *et al.*,2007, A&A, 469, 387
Thomas *et al*, 2005, ApJ, 631, 906
Turon C., Réquième Y., Grenon M. *et al.*, 1995, A&A 304, 82
Udalski A., Szymański M., Kaluzny J. *et al.* (OGLE Coll.), 1993, Act. Astr., 43, 289
Udalski A., Zebrun K., Szymański M.,*et al.* 2000a, Acta. Astr. 50, 1
Udalski A., Szymański M., Kubiak M.,*et al.* 2000b, Acta. Astr. 50, 307
Weingartner J.C., Draine B.T., 2001, ApJ, 548, 296